12-2010

Application of Ultrasound for Bubble Measurement in Water and Mercury

Hiraku Nakamura
University of Tennessee - Knoxville, hiraku@utk.edu

To the Graduate Council:

I am submitting herewith a thesis written by Hiraku Nakamura entitled "Application of Ultrasound for Bubble Measurement in Water and Mercury." I have examined the final electronic copy of this thesis for form and content and recommend that it be accepted in partial fulfillment of the requirements for the degree of Master of Science, with a major in Nuclear Engineering.

Arthur E. Ruggles, Major Professor

We have read this thesis and recommend its acceptance:

G. Ivan Maldonado, Jason P. Hayward

Accepted for the Council:
Carolyn R. Hodges

Vice Provost and Dean of the Graduate School

(Original signatures are on file with official student records.)

To the Graduate Council:

I am submitting herewith a thesis written by Hiraku Nakamura entitled "Application of Ultrasound for Bubble Measurement in Water and Mercury." I have examined the final electronic copy of this thesis for form and content and recommend that it be accepted in partial fulfillment of the requirements for the degree of Master of Science, with a major in Nuclear Engineering.

Arthur E. Ruggles, Major Professor

We have read this thesis
and recommend its acceptance:

G. Ivan Maldonado

Jason P. Hayward

Accepted for the Council:

Carolyn R. Hodges
Vice Provost and Dean of the Graduate School

(Original signatures are on file with official student records.)

Application of Ultrasound for Bubble Measurement in Water and Mercury

A Thesis Presented for the
Master of Science Degree
The University of Tennessee, Knoxville

Hiraku Nakamura
December 2010

ACKNOWLEDGEMENTS

I owe my deepest gratitude to my research advisor, Dr. Arthur E. Ruggles for his enduring patience, numerous advice and continuous financial support. I would also like to thank Bernie Riemer, Mark W. Wendel, and David Felde of the High Power Target group at Oak Ridge National Laboratory. Lastly, I am grateful for all the assistance Stuart Walker has provided.

ABSTRACT

Spallation Neutron Source at Oak Ridge National Laboratory is a neutron source operating with a liquid mercury target. Pulsed energy deposition in the target from the proton beam causes pressure waves that limit operation due to cavitation damage on the target container. Damage mitigation is proposed through the introduction of a 0.5 per cent gas volume fraction of small diameter bubbles to create compressibility in mercury. Desired bubble diameter is 30 micrometer, and two ultrasonic methods are studied for detection and characterization of such bubbles. These methods are tested first in water, and then in mercury. Ultrasound Doppler velocity profiler directly measures bubble rise velocity, which is then used to determine bubble diameter. Ultrasonic imaging allows direct observation of the bubbles both in water and in mercury. However, challenges were encountered in medical ultrasound image optimization and interpretation for this engineering application. This research explores techniques for implementing ultrasound in opaque fluids for bubble rise velocity and diameter characterization.

TABLE OF CONTENTS

LIST OF FIGURES

LIST OF ATTACHMENTS

1. homogenization.avi

Chapter 1 : INTRODUCTION

1.1 Background

The Spallation Neutron Source (SNS) is a linear accelerator (linac) driven high-flux neutron source located in Oak Ridge National Laboratory. Neutrons interact with materials and are advantageous for studies in various fields such as medicine, material science, and fundamental physics.

The SNS works by accelerating negative protons (H-) up to 1 GeV in a linac followed by an accumulator ring. The electrons are stripped to produce protons (H+) which are then deposited onto a liquid mercury target in pulses of duration of 1 μs, at a frequency of 60 Hz. The target mercury flows in a stainless steel vessel shown in Figure 1.1. Currently, the proton beam on the target is 1.4 MW with power upgrade levels into the 2 to 4 MW range [1]. The neutrons from the target are moderated before entering at the designated research beam line.

Figure 1.1: SNS target vessel [2].

Mercury was selected over water-cooled solid targets based on a technical study for the European Spallation Source [3] [4]. Some of the reasons a flowing mercury target is preferred include increased heat dissipation capability, nonexistent radiation damage and good production of neutrons [5] .

Due to the high thermal energy deposition per proton pulse, pressure waves are generated and propagate throughout the system [6]. The interaction of the target holder wall with pressure waves in the mercury results in cavitation damage [7]. Early studies determined the target holder endurance as a function of the operational time and power level, and the target lifetime was expected to be limited by this damage mechanism. In order to reduce the damage rate, compressibility is increased in liquid mercury by injection of Helium microbubbles. The low solubility of gas in mercury helps make cavitation damage mitigation using microbubbles viable [8].

Bubble detection and diameter distribution characterization is required to ascertain success of the bubble generation approaches. Conventional optical means of detection and characterization of bubbles do not work in opaque mercury. This study presents the application of ultrasound to characterization of bubbles in mercury.

1.2 Organization

The goal of creating compressibility in the mercury target using Helium bubbles requires measurement methods for Helium bubbles in mercury. A review of ultrasound application in both industry and medicine is offered in chapter one to show viability of ultrasound imaging to the bubble measurement opportunity. Chapter two describes the experiments and equipment used for exploring techniques for bubble measurement, and for bubble production. Experiments were performed in water and mercury with measurements taken using the Ultrasound Velocity Profiler (UVP) and a medical Ultrasound (US) imaging system. Chapter three presents results of UVP and US imaging experiments for bubbles in both water and mercury. Chapter four reviews the highlights of the entire thesis and proposes areas of future research.

1.3 Literature Review

Flow behavior and trajectories of bubbles and particles in the flow are of importance to numerous industrial processes. Optical methods such as laser Doppler anemometry (LDA) and particle image velocimetry (PIV) are often used to characterize such flow. However, opaque fluids require use of alternative techniques that use x-rays, electromagnetic radiation and neutrons to examine the flow. X-ray PIV has imaged velocity fields through opaque objects with reasonable agreement to theory [9]. Density field visualization using an X-ray beam in liquid metal has worked with difficulty noted obtaining high resolutions at the interface locations [10]. High speed flow visualization of air bubbles rising in water was demonstrated using neutron radiography through an aluminium alloy channel [11]. Static and video images of bubbles in various mercury flow conditions have been shown using proton radiography [12]. Two dimensional chord density measurements all have difficulty resolving the interfacial edge of the three dimensional bubble, thus limiting accurate volume measurements of small bubbles.

Other evaluation methods have been developed to characterize and detect discontinuities in various materials. One frequently used evaluation method for finding defects and discontinuities is ultrasonic testing [13]. The basis for nondestructive evaluation using ultrasound was established by Firestone during the 1940s [14]. Ultrasonic testing employs high frequency pulses ranging from 0.1 MHz and at times in excess of 100 MHz for evaluating the material properties and flaws. Note that sound in steel at 100 MHz has wavelength equal 60 μm and in water this wavelength is 14 μm.

Ultrasonic testing detects the presence and location of discontinuities either by echoes or the attenuation. In addition to time and intensity measurements, shifts in frequency have also seen used. Axial velocity measurements can be taken using a single element ultrasound device that employs Doppler shift (e.g. Met-Flow UVP) to measure the velocity of targets returning echoes in the flow field [15]. UVP velocity measurements have been shown to be highly accurate when solid targets are employed [16].

The medical community has long used ultrasound in both imaging and treatment applications. Frequency ranges of 1 MHz for deep structures to 20 MHz for superficial structure are routinely used. The ability of ultrasound to propagate through transparent and opaque fluids makes it a versatile method. The successful application of ultrasound

imaging arrays in the medical industry is applied to engineering flow measurement in this research.

The first medical use of ultrasound is attributed to John Wild in 1949 [17]. Characterization of ultrasound in tissue was first reported in 1958, laying the foundation of medical imaging [18]. In 1963 the first commercial B-mode scanner was released [19]. B-mode stands for Brightness mode in which the brightness of a dot is modulated based on the amplitude of the reflected signal. The brightness of the dot displayed to the user represents the signal strength. The depth of the object from the transducer is represented by the position of the dot. With advances in solid-state technology, scans became 2-D images of echo strength in the position field.

Ultrasound imaging of circulatory systems in animals has been improved through the use of contrast enhancing agents which use small bubbles to add compressibility to the blood flow. These techniques were solely investigational as recently as 1990's, but are currently a conventional technique for human circulatory system imaging. The microbubbles injected into the blood stream are most commonly used in echocardiography to improve visualization of cardiac chambers. These microbubbles are comprised of two components; the shell and the fill-gas. The shell is made of an elastic material such as albumin, lipid, or polymer which encapsulates the gas and resists bursting from the acoustic energy of the ultrasound. Microbubbles are commonly filled with air, nitrogen, octafluoropropane C_3F_8or perfluorocarbon with diameters ranging from 1 to 6 μm [20]. Medicine takes advantage of two important features of microbubbles. One being the rheology of microbubbles is nearly identical to red blood cells allowing for diagnosis of abnormal flow [21]. Another feature is the disruption of the bubbles using high-power ultrasound [22]. The outer encapsulation of bubbles may carry a drug, allowing high power ultrasound to disrupt the bubble and deliver the drug to a desired location [23].

Two-dimensional imaging in medicine is standard practice, with 3-Dimaging increasingly becoming routine for the fetus. In addition to the three spatial dimension of 3-D US, 4-D US incorporates temporal resolution thus making it a real-time 3-D US. Current hardware allows the medical US operator to experience the image in 3-D using high-definition monitors along with special 3-D glasses.

Chapter 2 : METHODS

2.1 Ultrasonic Velocity Profiler (UVP)

2.1.1 Method of Operation

The UVP measures the velocity of targets using the Doppler shift in an echo from a transmitted ultrasound wave. A single element US transducer transmits a short pulse and then switches to a passive mode of listening for return echoes. Figure 2.1 represents a typical US beam as it emits from the transducer face.

The UVP measures Doppler shift in signed 127 (255 unsigned), i.e. positive or negative, channels with equal channel width. The Doppler shift is converted to true velocity V by:

$$V = \frac{c\Delta f}{2 f_0} \tag{1}$$

where Δf is the frequency shift due to the Doppler effect, c is the speed of sound in the medium, and f_0 is the ultrasound frequency. The speed of sound though a dependent variable, is taken as a constant that the user designates before running the UVP.

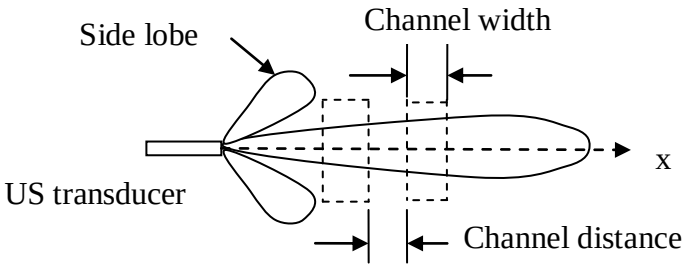

Figure 2.1: Single element UVP transducer beam (not to scale).

The channel width *w* is given by:

$$w = \frac{n\lambda_0}{2} \tag{2}$$

where *n* is the number of cycles and $\lambda_0$is the transmitted wavelength.

The maximum detectable target velocity is limited due to the Nyquist sampling frequency as:

$$V_{\max} < \frac{cf_{prf}}{4f_0} \tag{3}$$

where f_{prf} is the pulse repetition frequency.

The existence of side lobes (Figure 2.1) can result in artifacts if the intensity is not 60 to 100 dB below that produced by echoes in the main beam [24] [25]. A number of echoes may be collected from each measurement volume to provide a time averaged axial velocity value for that measurement region.

2.1.2 Met-Flow – Commercial UVP

UVP hardware comprises a computer, monitor, user interface (mouse and keyboard), and transducer digital signal processor all in a portable unit shown in Figure 2.2. The UVP-XW software provides real time data with user controlled parameters such as speed of sound in the medium, orientation of the transducer, and spatial resolution. The result of the measurement is directly saved on to the computer hard drive in binary format which can be retrieved using a 1.44 MB floppy disk. It is also possible to covert the data file into a more universal format such as text. US transducers range from 0.5 to 8 MHz with typical frequencies being 2, 4, and 8 MHz. Multiple transducers may be used through an integrated multiplexer.

Figure 2.2: Met-Flow UVP

2.1.3 UVP Experimental Setup

UVP requires seeds to detect returning echoes. Seeds in UVP experiments described here are bubbles produced through homogenization of larger Helium gas bubbles as shown in Figure 2.3. This figure describes the bubble production method inside a cylindrical tank. The seed bubbles were generated using a laboratory homogenizer (Cole Parmer Lab GEN 700) commonly used in life sciences to disrupt cells. Helium gas was directly released under the homogenizer tip where the gas is sheared by the rotating tip into sub-millimeter bubbles. A still image of the bubbles from the homogenizer is provided in Figure 2.4. A video file (homogenization.avi) is also available along with the original electronic thesis.

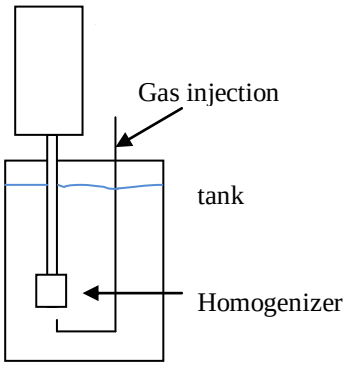

Figure 2.3: Schematic of bubble production using homogenizer.

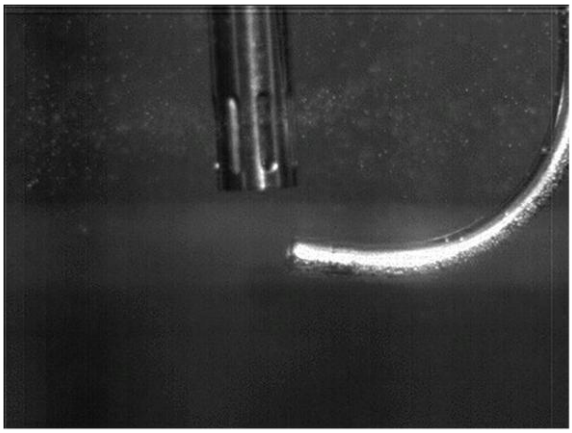

Figure 2.4: Image of bubbles produced by homogenizer in water.
Homogenizer tip diameter is 8 mm.

Bubble generation in mercury employs the same technique as described above with the fluid being mercury. Figure 2.5, shows the tank of mercury (nearly 2 L) inside a fume hood. The vessel lid has the homogenizer with the motor removed, 4 MHz angled transducer, gas vent line, Helium injection line, and mercury inlet. The transducer was angled due to previous experience of bubbles accumulating at the tip of the transducer when positioned vertically. Bubbles on transducer surface reduce acoustic transmission and reception between the transducer and mercury.

Figure 2.5: Angled transducer design ready for mercury experiment inside fume hood.

2.2 Medical Ultrasound Imaging

2.2.1 Image Formation

Ultrasound image formation involves three major steps. The first process involves the generation of ultrasonic wave for transmission using a piezoelectric transducer head comprised of an array of 128 piezoelectric elements. The sound wave propagates from the head through the medium after the generation of the wave, and the same head listens for returning echoes. The final process captures the returning echoes from all elements in the head and processes the signals into an image.

An image is constructed based on the time taken for echo return and the strength of the echo. The time taken between the transmission of a pulse to the reception of the echo determines the distance from the US probe. The signal strength is encoded into 8 bit grayscale image where 0 represents no signal (black) and 255 represents the upper most threshold (white).

An issue with electronic arrays is the existence of secondary lobes (Figure 2.6) appearing beside the main beam [26]. The side lobes are due to interference patterns, the same physics that creates side lobes in the UVP probe. These side lobes can cause artifacts in the US image. The lateral resolution is improved by applying synthetic aperture focusing techniques (SAFT). Unlike the tradition means of using an ultrasonic lens, which functions like an optical lens and drastically reduces the transmitted signal, SAFT corrects the image based on a known model of the beam transducer phase response. Correlating the signals to known target positions enables a corrected image.

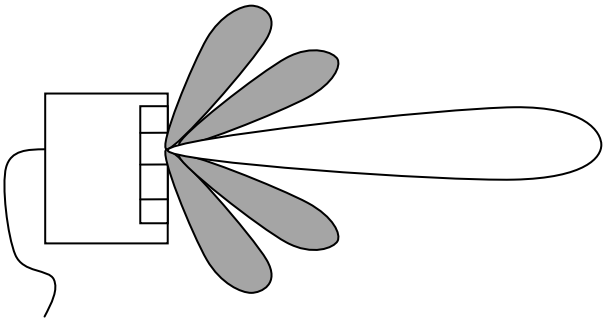

Figure 2.6: Linear array with side lobes (shaded) at various angles to the main beam.

2.2.2 Terason – Commercial Medical Ultrasound System

The ultrasound imaging probe used here, a Terason 12L5V, has 128 elements, in two rows, and the transducer array is activated to produce a sweeping beam. Unlike most medical ultrasound on carts commonly used for clinical purposes, the Terason is a portable unit (Figure 2.7). In combination with a laptop running the Terason software, the hardware with the US probe is powered by a single IEEE 1394 cable. This cable also transfers data for real time imaging at about 30 frames per second (fps). Both still and motion images can be acquired on demand for a specified duration (usually 3 seconds). The data is saved in a format specified in the Digital Imaging and Communications in Medicine (DICOM). DICOM is the standard format used in the medical community which contains various information of the device, its parameters and image attributes in addition to the 8-bit grayscale image itself.

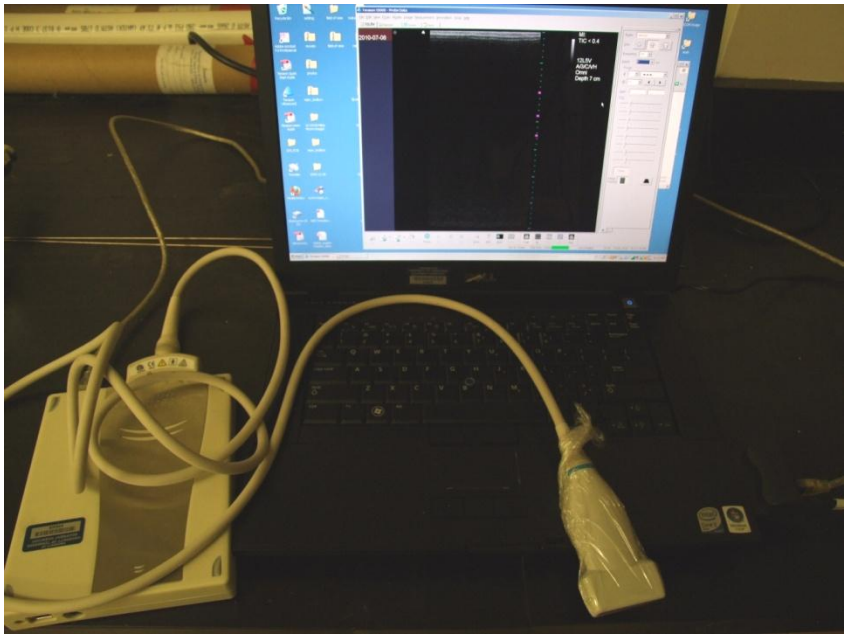

Figure 2.7: Terason t3000 with 12L5V probe with US software running on the laptop.

A typical three-second DICOM file is approximately 70MB, totaling nearly a gigabyte of data per experiment. In addition to the default DICOM format, it is also possible to export the image as an AVI or JPEG file. However such file conversion will entail a distortion of resolution and information as these formats are compressed. All DICOM images shown were reconstructed using a custom MATLAB script (Appendix C).

2.2.3 Imaging Parameter and Control

Ultrasound imaging outcomes are user-dependent. The quality of the image and the capability to correct the image requires optimization of control parameters and careful probe positioning and probe acoustic coupling to the media. The major parameters of interest are scan mode, frequency, depth, focus, gain and time gain compensation.

As with standard ultrasound imaging, the Terason unit is equipped with two distinct imaging modes which can be categorized into 2-D imaging and Doppler mode. The 2-D mode (B-mode) provides a plane image such as Figure 2.8. The M-mode stands for “motion” in which the scan shows motion of the object along an axis during the 2-D mode, as shown in Figure 2.9. Power Doppler mode is designed to display velocity of red blood cells in the blood flow.

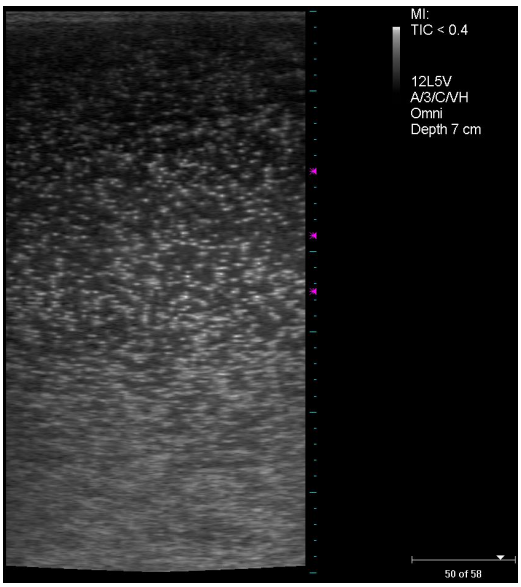

Figure 2.8: Microbubbles in water.

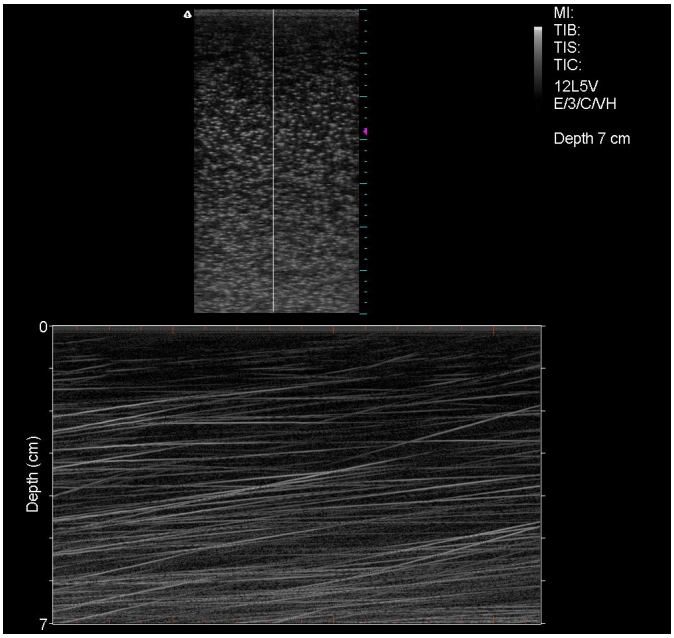

Figure 2.9 Use of M-mode on rising bubbles with time span of 3 sec.

Terason allows the user to select the exam type (e.g. ventricle) for the anatomical structure of interest. This selection imposes predefined setting which can be altered during operation. In addition to exam type selection, patient body size maybe chosen from small, medium, and large. This changes the frequency and ultrasound penetration depth. Selecting small body size sets the frequency to high and depth to shallow and the opposite for large body size. The user may override all predefined settings. However it is important to note that the description of these controls lack quantification and at best one can only presume the actual value. For example, selecting “VH (very high)” for frequency is presumed to be at 12 MHz, the maximum operating frequency of the ultrasound probe.

Ultrasound penetration depth is adjusted based on frequency and at “VH” frequency the maximum depth is 7 cm. One key feature for image quality is the focus setting which is comprised of the number of focus locations, the depth, and distribution of focus. Generally, the number of focus points is set to 1 and no more than 3 with the distribution set to dense and depth set to location of the object of interest. The best results have been with the depth set around the middle range at approximate 3 to 3.5 cm.

Gain control enables the amplification of the echo shown by the intensity in grayscale. In imaging bubbles, lowering the default gains generally improve the overall contrast of major bubbles. However, smaller bubbles will appear as echoes with similar strength to background noise. Another key parameter for improving image quality is the Time Gain Compensation (TGC). TGC allows for gain to be adjusted at certain depths to compensate for attenuation of the signal. TGC must be increased in the region where bubbles exist since attenuation is high through bubble groups.

2.2.4 Ultrasound Preliminary Experiment

Ultrasound imaging of bubbles using the Terason probe was initially done in water due to the ability to compare image outcomes with optical observations. Subsequent test were performed in mercury. In proceeding with ultrasound experiments, the probe was tested for imaging capability through sheets of Lexan, acrylic and stainless steel. These test required the use of a contact medium to couple the ultrasound signal from the transducer to the media of interest. A gel pad (Figure 2.10) or acoustic gel was used in these tests.

As a preliminary test of the conforming gel pad, bubbles suspended in the acoustic gel bottle, shown in Figure 2.11, were imaged. The test assessed the conforming gel pad's ability to create sufficient contact between the flat transducer face and the cylindrical surface of the bottle.

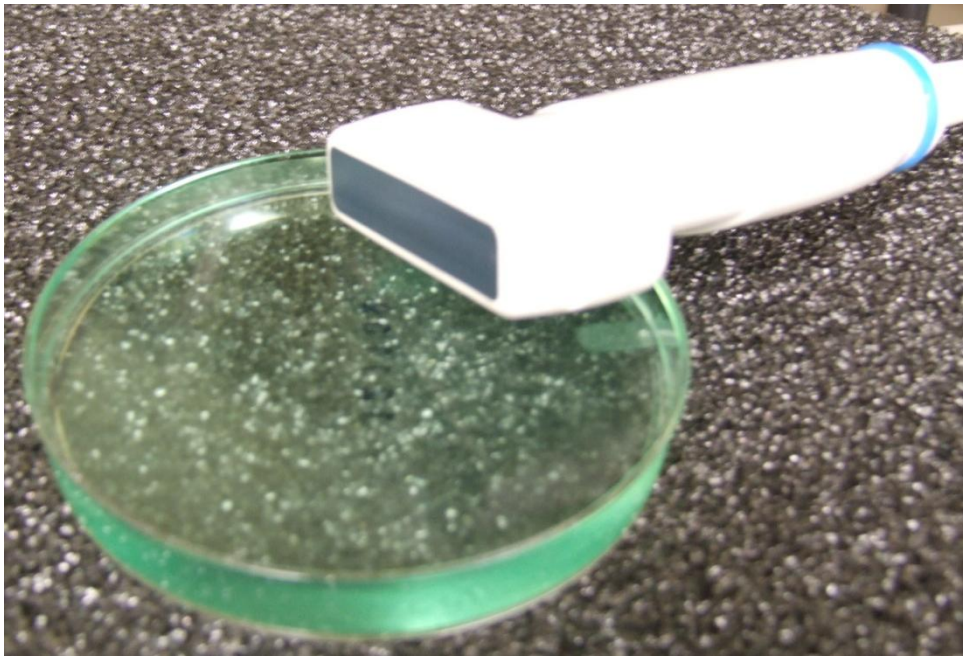

Figure 2.10: Conforming gel pad (1.5 cm thick) with US probe

Figure 2.11: Bubble imaging test using the conforming gel pad

Figure 2.12 shows the bubble image taken at VH frequency with depth set at 5 cm based on the exact condition seen in Figure 2.11. The top layer, approximately 0.8 cm

in depth, is the gel pad and the bottom streak is the opposite side of the bottle. The apparent thickness of the pad seen in the Figure 2.12 is of 0.8 cm, while the actual thickness is 1.5 cm. This variation is partially attributed to the compression necessary to maintain contact between the surfaces.

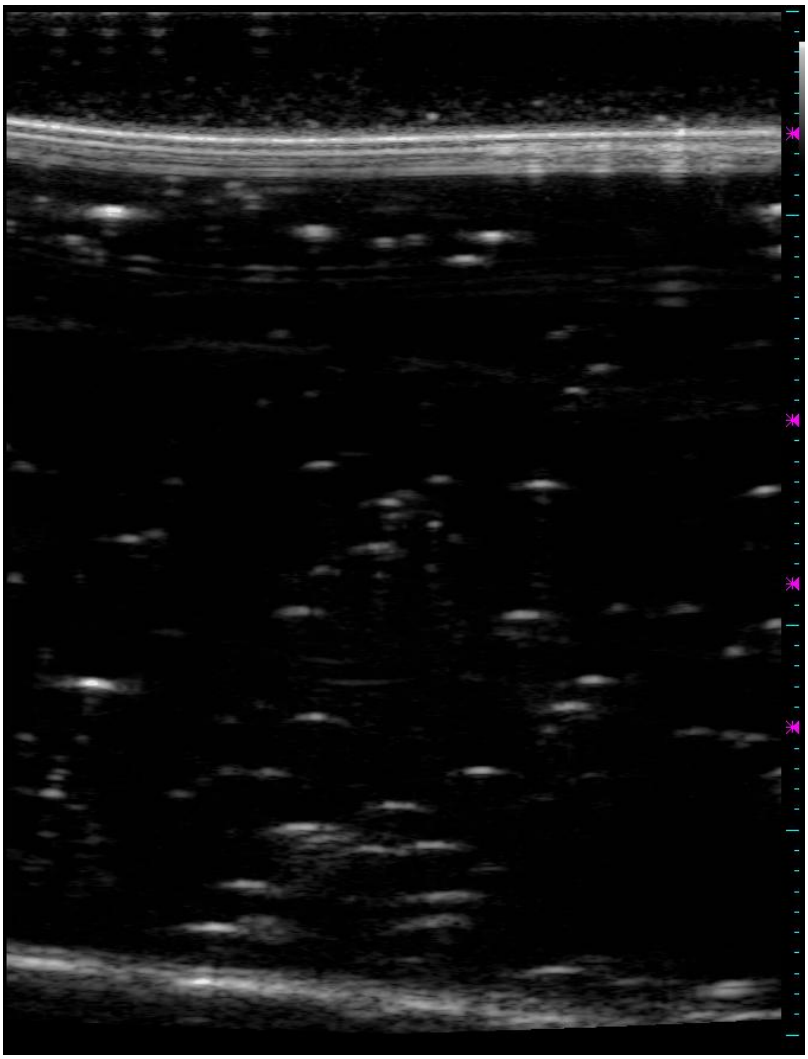

Figure 2.12: US image of bubbles in acoustic gel.

2.2.5 Ultrasound Experiment: Mercury Loop Schematic

The schematic of the microbubble experiment in mercury is shown in Figure 2.13. The motor is couple to a pump housed inside a mercury tank which exits the tank through the blue line. Mercury enters the microbubbler along with Helium gas producing microbubbles inside a tank of mercury before returning (Figure 2.13, green line) into the original tank.

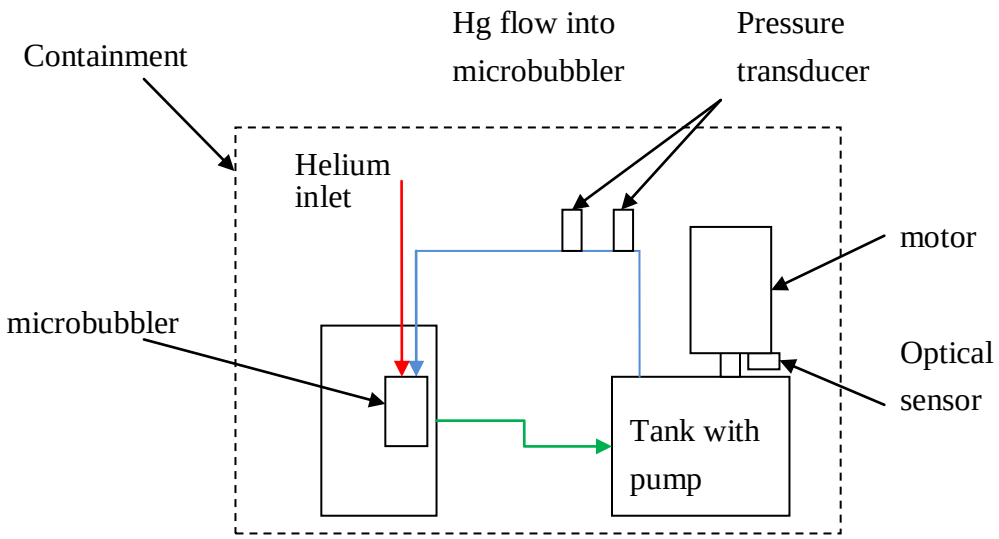

Figure 2.13: Schematic of mercury loop with test section on left.

2.2.6 Ultrasound Experiment: Data acquisition

This mercury loop has two pressure transducers and one optical sensor attached. Figure 2.14 shows the data acquisition system with a laptop running LabVIEW. The schematics for the custom data acquisition system is shown in Figure 2.15. Two different power supply units are used since the pressure transducers require 24 V, whereas the optical sensor uses 10 V. The return signal is a voltage value up to 5V for the pressure transducers, which is converted to a pressure based on supplier specification. The optical sensor returns a 5 V square wave with varying frequency which is processed to yield the revolution of the motor per second. Output signals were read and converted digitally by National Instruments USB-6211 data acquisition (DAQ) unit connected to a laptop running LabVIEW. The block diagram used for this mercury loop is shown in Appendix A.

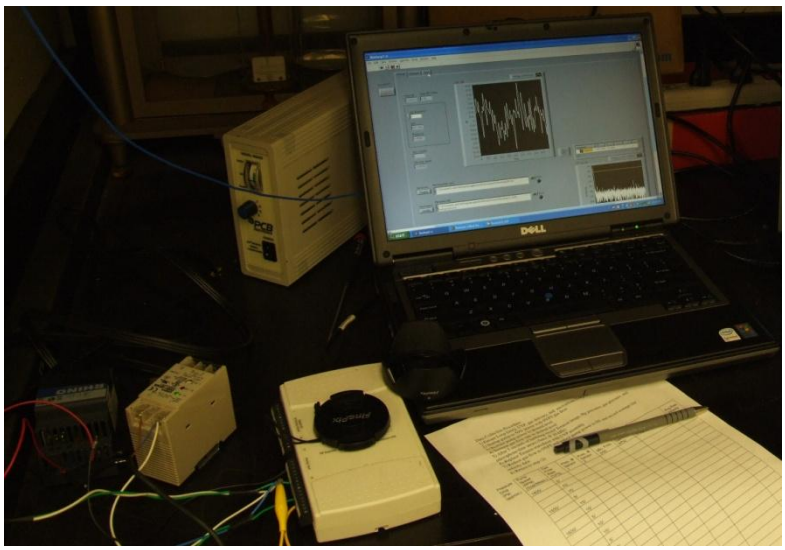

Figure 2.14: Data acquisition (DAQ) using LabVIEW on laptop.

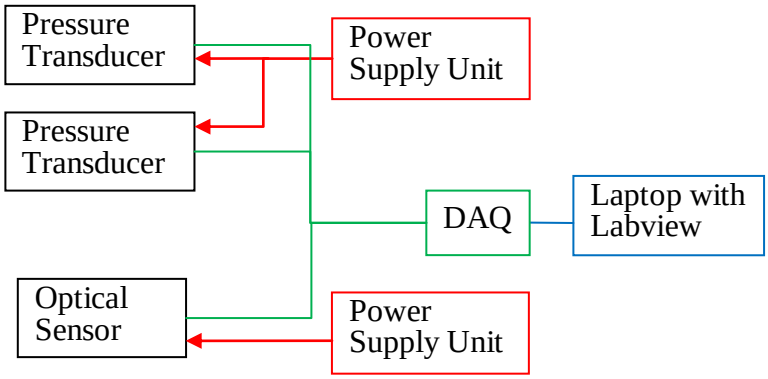

Figure 2.15: Schematic of data acquisition (DAQ)

Complications were encountered during the integration of pressure sensors into the flow loop. Attempts to isolate and diminish the noise were the most challenging and time consuming aspects of the loop build process. Strong noise reading (SNR ~0.1) made sensor output difficult to isolate. The major source of noise was the 240 V variable speed motor creating potentials of 80 V between the system (partly due to the conductivity of mercury) and the sensors. This noise was attributed to use of the silicon controlled rectifier (SCR) variable speed control for the pump motor, and later research revealed this kind of noise problem with SCR controls is common.

2.2.7 Ultrasound Experiment: Mercury Loop and Microbubbler

Initial explorations of US imaging of bubbles in water used bubbles generated by direct injection of helium using 1/8 inch tubes. The US probe was placed over the rising bubbles for imaging. Subsequent endeavors utilized a microbubbler that produced bubbles less than 100 μm in diameter inside a large water tank [27].

The latest mercury loop configuration includes a stainless steel microbubbler which was extended to be housed inside mercury filled tank. Figure 2.16 shows the extended microbubbler with a custom acrylic lid.

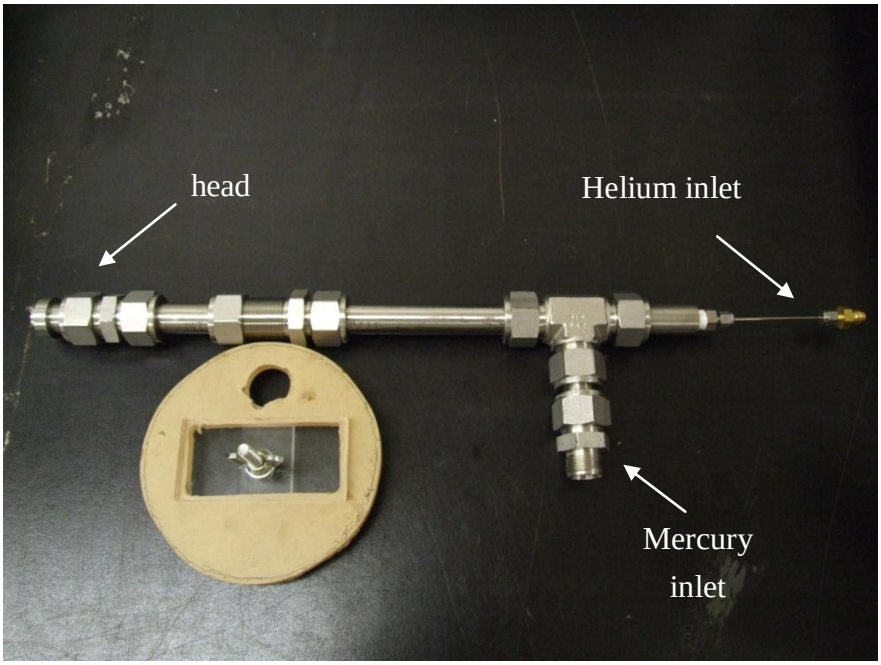

Figure 2.16: Elongated microbubbler with lid.

The toxicity of mercury was respected through use of three layers of containment. First containment is the actual vessels in which it is sealed with a carbon filtered vent. Second is the acrylic box as seen in Figure 2.17 which also has a carbon filter with vacuum pump. The third containment is the fume hood which ran throughout the experiments. Gloves, lab coats and eye protection were also used when the flow loop was opened in the hood for service and reconfiguration.

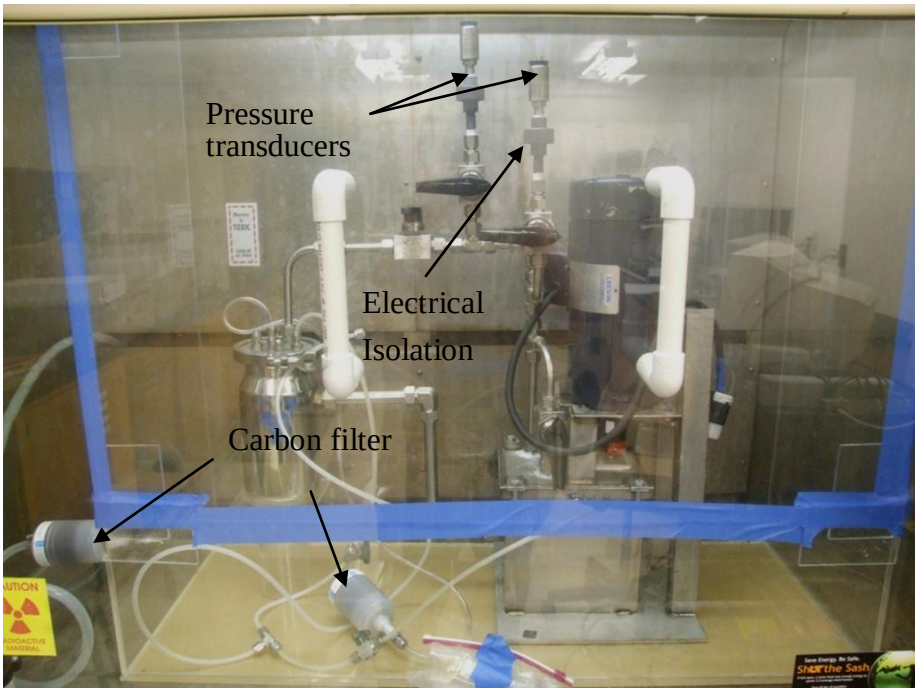

Figure 2.17: Mercury loop in a sealed containment box inside fume hood.

Microbubble generation in mercury is shown in Figure 2.18 based on an experiment procedure (Appendix B) which involves the refitting of the stainless steel tubes with the microbubbler. The experiment required an open surface since the US probe needs to be placed directly over the mercury surface for imaging. The experiment was executed in a timely manner as mercury vapor can form inside the hood. Mercury vapor was monitored before and after the experiment as detailed in the procedure.

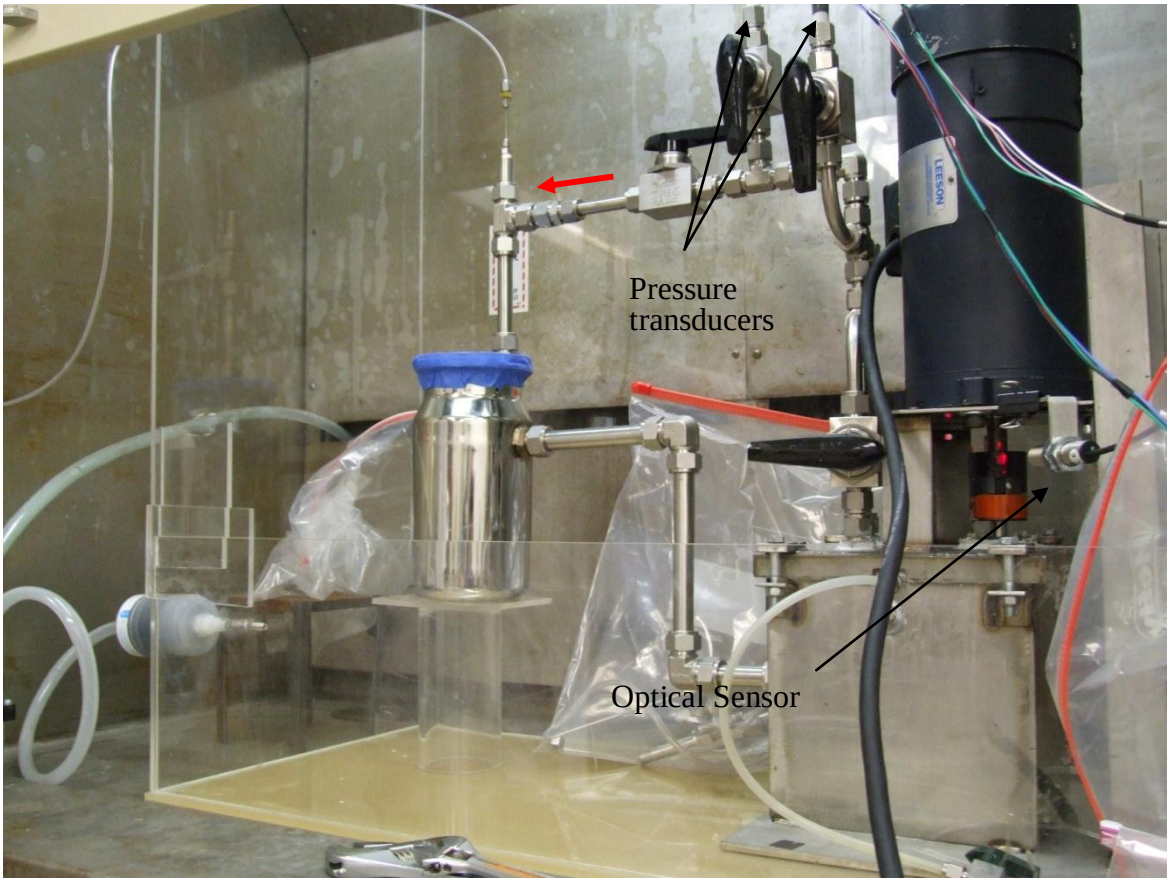

Figure 2.18: Mercury loop in operation.

2.3 Field of View characterization

2.3.1 Ultrasound Image Distortion

Ultrasound imaging of the 12L5V probe was checked against actual physical dimensions in B-Mode. Figure 2.19 show the layout of the wire and metal bead setup used for these evaluations. Two beads rest on fishing wires at a depth of 7 cm. The image field is 403 pixels wide and 757 pixels high; about 11 pixel/mm for both directions. The base US field (Figure 2.19, red) has dimensions 37.3 mm by 12 mm (width, thickness). The dimensions were measured by distancing the metal beads until both

beads were out of view. Figure 2.20 shows the magnified view of the metal bead used with respective dimensions.

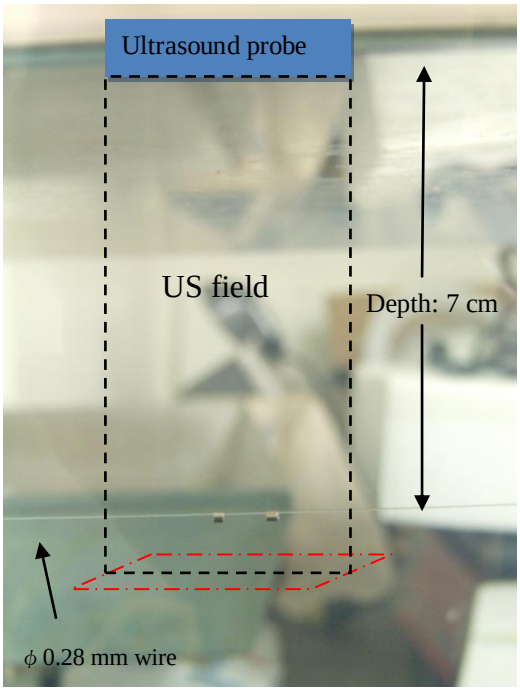

Figure 2.19: Side view of ultrasound field mapping apparatus setup inside an aquarium.

Note: US field not to scale.

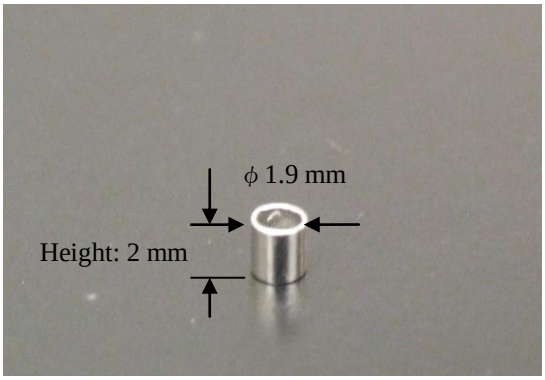

Figure 2.20: Magnified view of the bead

The Figure 2.21 is an image of two 2 mm beads on a wire. The scaling on the side (light blue marks) shows 7 major markings representing the 7 cm depth with the minor marks being 2 mm. This image leads one to view the wire as being a little less than 2 mm in diameter. However, the actual diameter of wire is 0.28 mm. The diameter of the wire on the image is approximately 14 pixels, which suggests that relatively small objects are represented in pixel sizes larger than actuality.

The US image Figure 2.21 shows the wire at depth equal to 6.5 cm from the US probe face. The actual depth was 7 cm from the probe face. The wire is shown 0.5 cm above the actual position. The Terason user guide notes a position error of 5% at depths greater than 50 mm and this is comparatively close to the observed discrepancy.

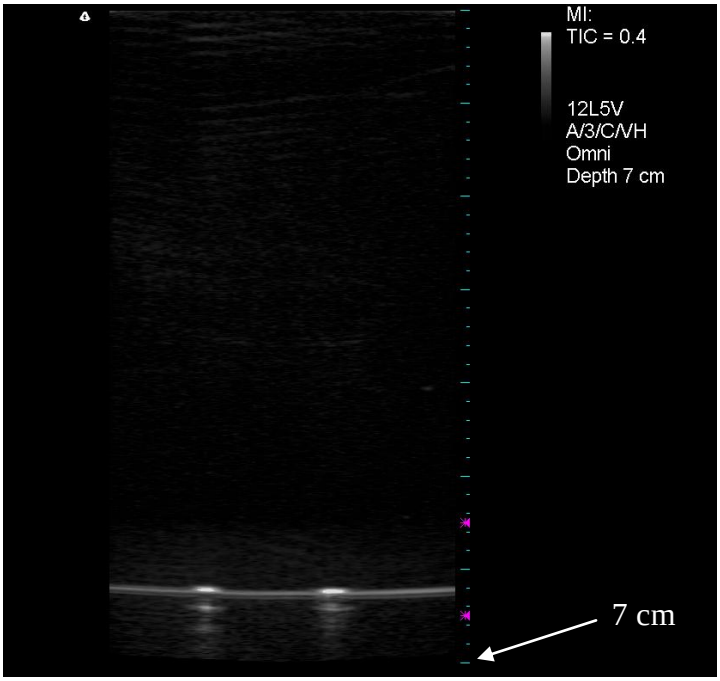

Figure 2.21: Wire with two metal beads

2.4 Particle Image Velocimetry

2.4.1Principle of Particle Image Velocimetry (PIV)

Particle Image Velocimetry (PIV) typically consists of tracer seeds, laser, camera and post-processing software. Figure 2.22, below shows the basic steps of PIV. The seeds are added to the flow on which the laser illuminates the imaging window. The seeds scatter the light for digital recording. At least two short laser pulses are made which is synchronized with the camera. The captured frames are post-processed by dividing the frame into small areas for the two sequences of frames. A comparison of each area is made by statistical methods (auto- or cross-correlation). The peak of the correlation corresponds to the displacement vector. The velocity field is calculated based on the displacement vectors and time between successive laser pulses.

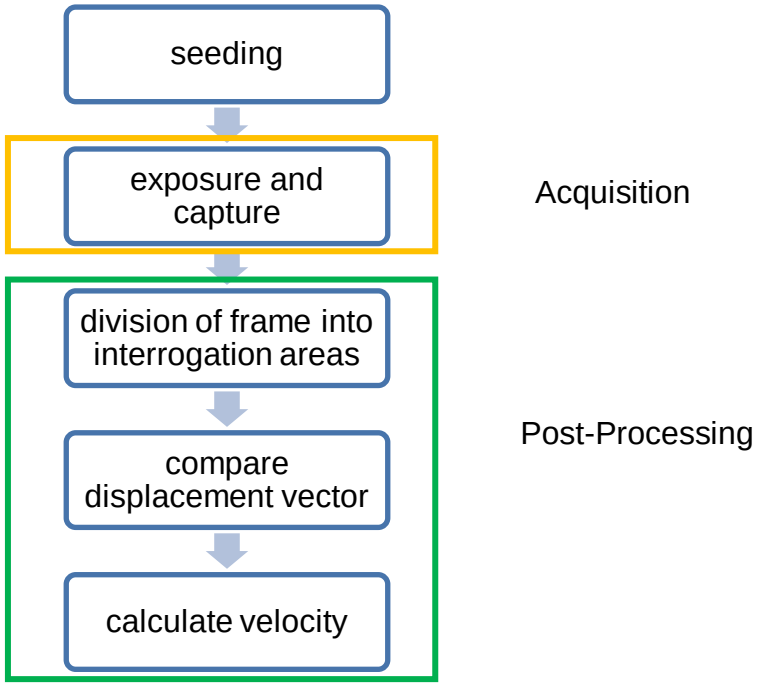

Figure 2.22: Typical steps of PIV method.

Several PIV software such as OpenPIV, mpiv, and URAPIV available online were tested for obtaining velocity fields from the dicom files. URAPIV (open source) was used as it required minimal effort obtaining velocity fields presented in this report.

URAPIV requires two sets of image files to calculate the velocity. A DICOM file with few bubbles (Figure 2.23) was used for the PIV process. This requires first the conversion of DICOM files into image files. The images must be named or ordered sequentially into pairs for comparison.

2.4.2 Image Treatment for PIV

Ten frames were used comprising 5 pairs with interrogation window of 16x16 pixels without any filter. This required approximately 2 minutes to process. Figure 2.23 is the original image with Figure 2.24 through Figure 2.26 being the first 3 fields of the 5 image sets processed.

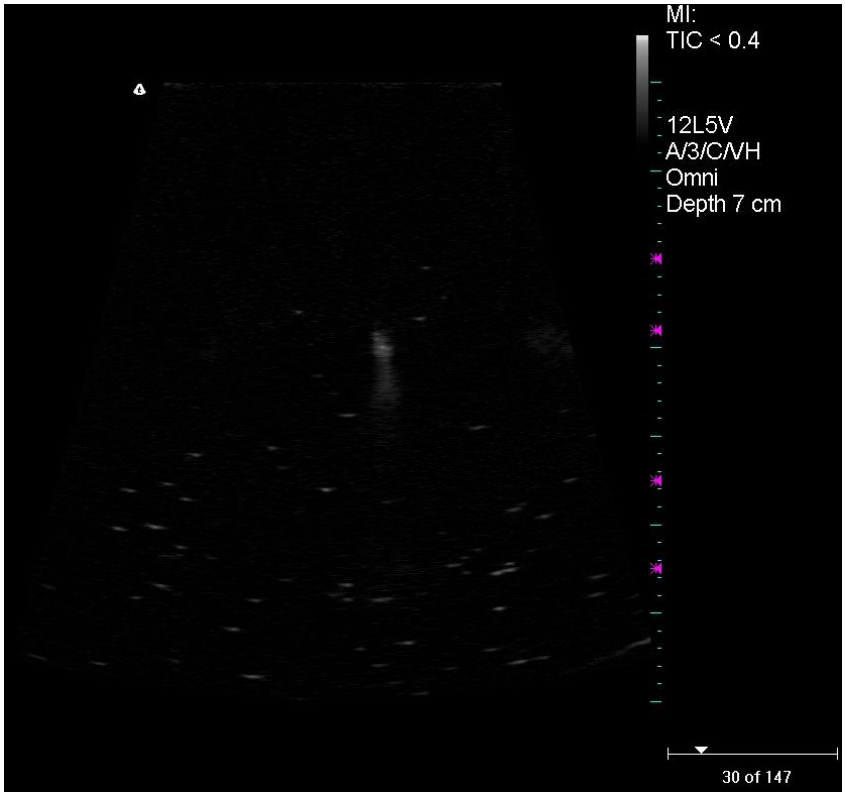

Figure 2.23: Original

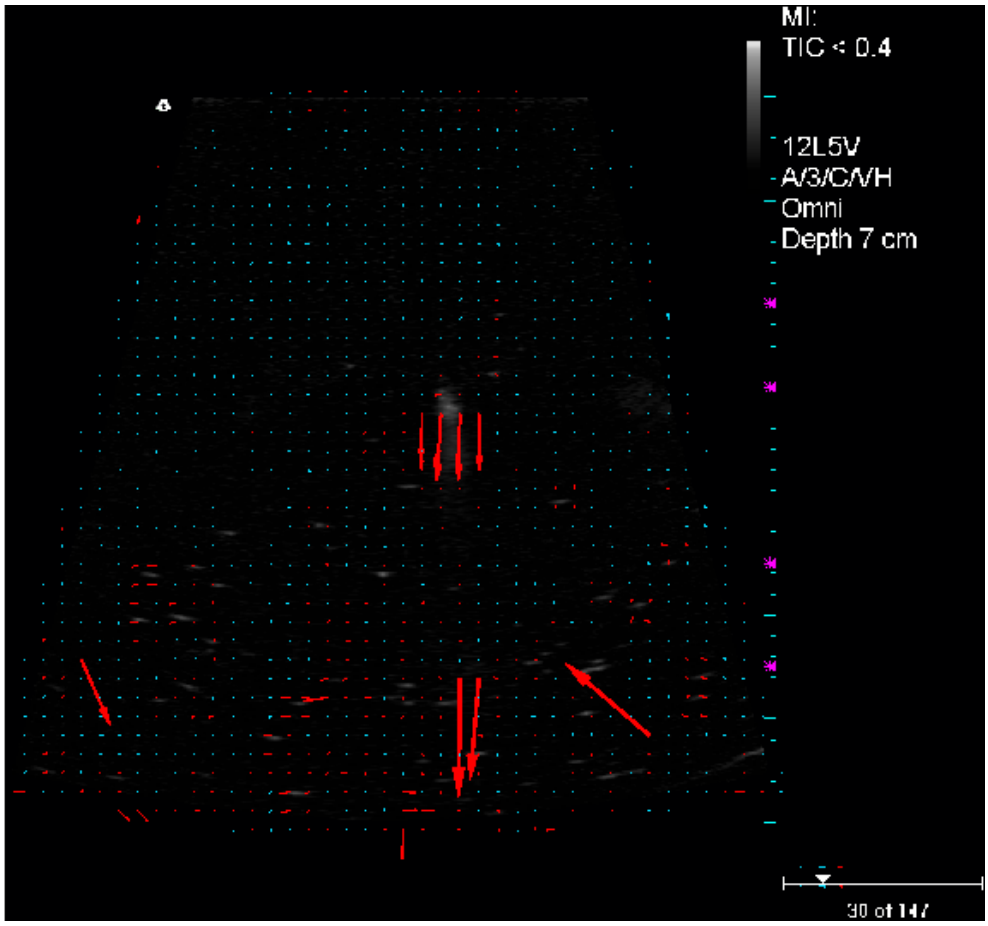

Figure 2.24: PIV results with vectors magnitude scaled 5 times the actual values. 1/5

The initial impression of the results was that the velocity fields had no obvious flow direction. Future analysis requires ultrasound image comparison to the high-speed videos of the microbubble movement. Currently long duration (> 3s) dicom files cannot be imported to MATLAB due to memory limitations. Flow patterns and bubbles are clearly recognizable upon visual inspection in both the dicom files and converted avi files. However, PIV method used here does not completely match human motion perception from the videos.

A combination of thresholding and filtering can improve the PIV outcomes, and an example of this is offered in Figure 2.27. Details of the conditions and bubble generation leading to Figure 2.27 are offered in Chapter 3.

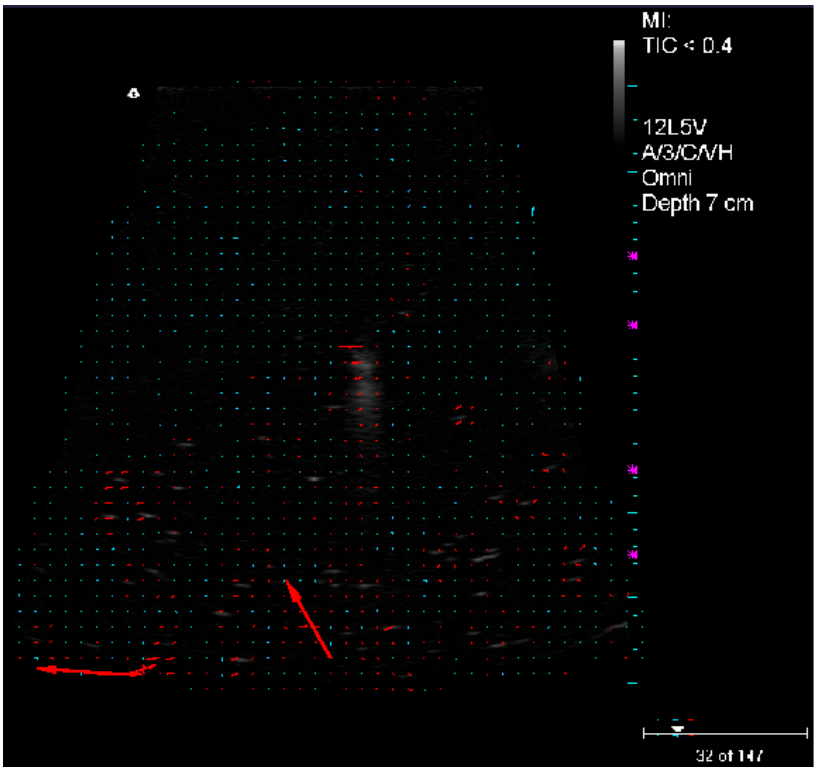

Figure 2.25: PIV results 2/5

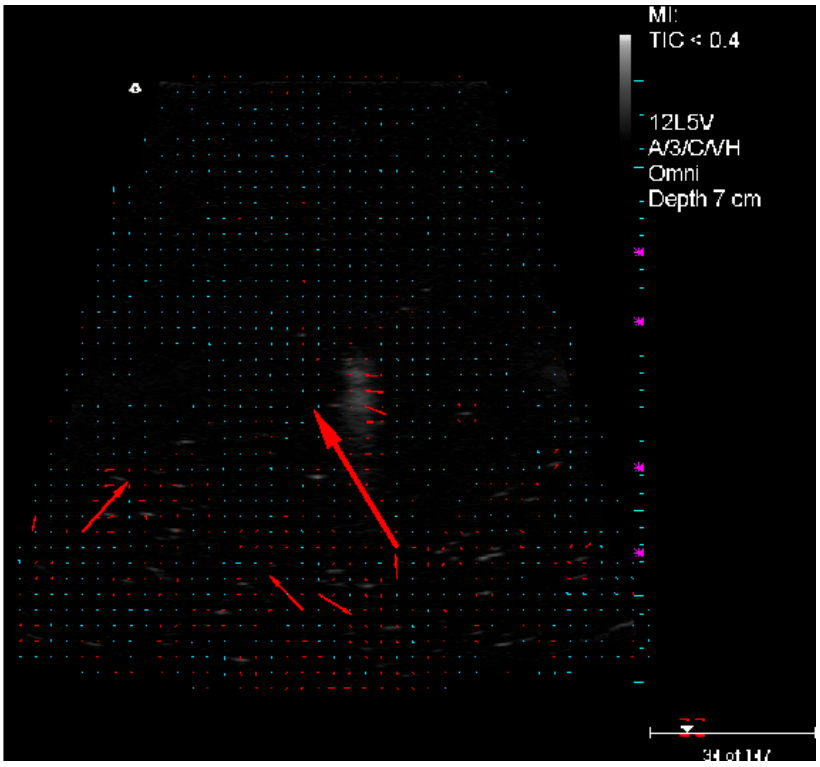

Figure 2.26: PIV results 3/5

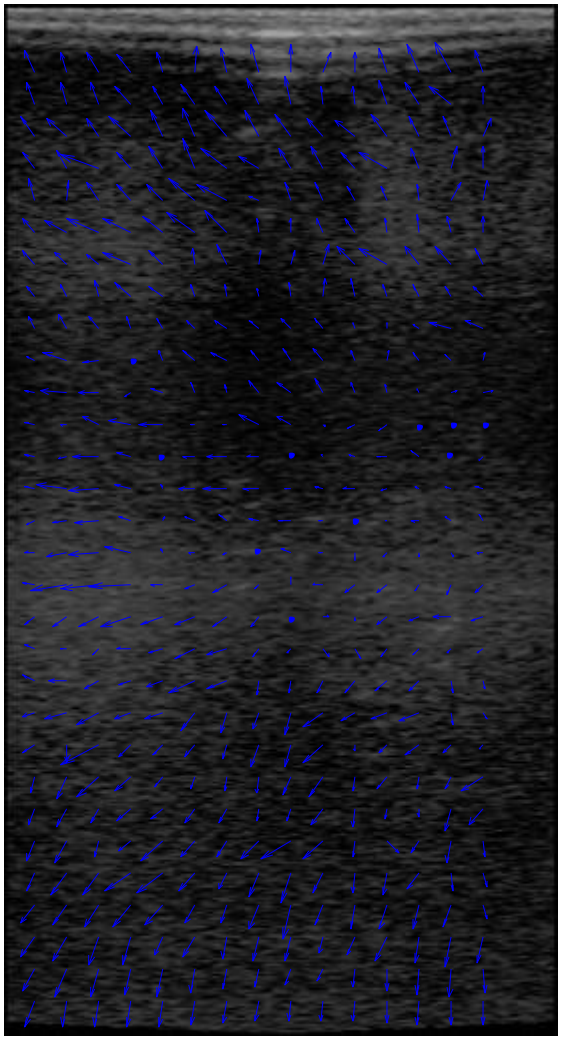

Figure 2.27: PIV based on the center and right frames of Figure 3.17.

Chapter 3 : RESULTS AND DISCUSSIONS

3.1 UVP

3.1.1 Bubble rise velocity: water

Helium bubble rise velocity profiles in water were taken using the experimental facility described in section 2.1.3 UVP Experimental Setup. Figure 3.1 represents the mean velocity taken over 1000 UVP profiles as a function of the distance from the transducer head. Due to the angled transducer the velocities near the transducer head are nearly zero as no bubbles are in the ultrasound beam. At a rise velocity of 30 mm/s the bubble diameter is approximately 0.2 mm based on Stoke's Law. This diameter decreases to 0.15 mm for rise velocity of 14 mm/s.

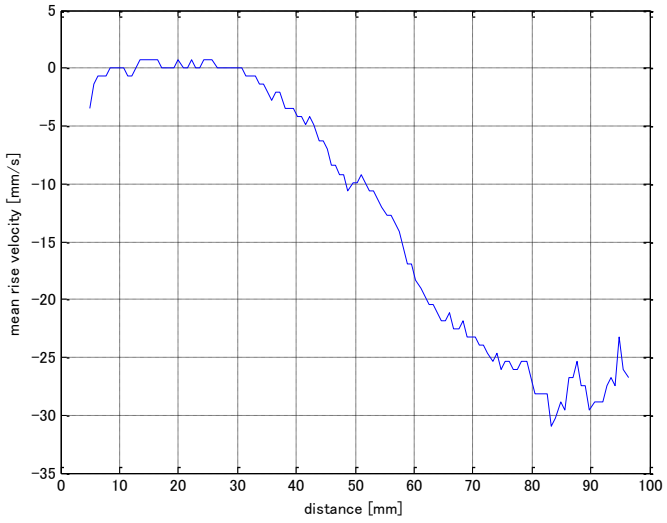

Figure 3.1: Bubble rise velocity in water averaged over a thousand profiles (approx. 15s).

3.1.2 Bubble rise velocity: mercury

Bubble rise velocity in mercury is shown in Figure 3.2, using the same method for bubble generation as for water. At a rise velocity of 60 mm/s the bubble diameter is approximately 0.1 mm based on Stoke's Law. The mercury data is also represented as a spatial-temporal plot with color intensity representing UVP velocity data in Figure 3.3. A thousand profiles were taken with each profile at 14 ms along 128 channels with each channel at 0.72 mm. The two white lines in Figure 3.3 represent the velocity of a group of bubbles moving through the gated axial measurement volumes. This offers opportunity to compare Doppler based velocity measurements with time of flight data embedded in Figure 3.3.

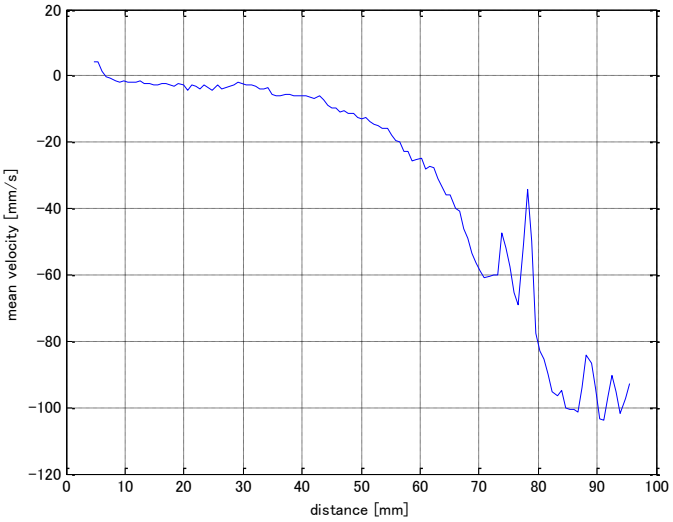

Figure 3.2: Bubble rise velocity in mercury averaged over a thousand profiles (approx. 15s).

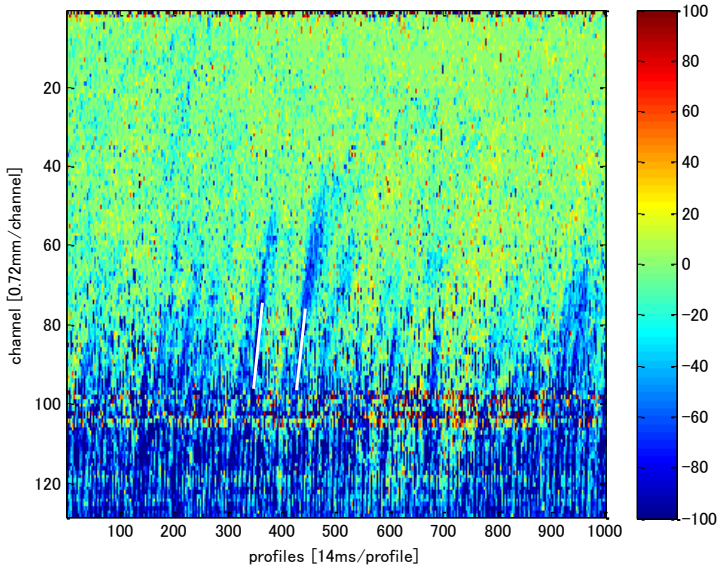

Figure 3.3: Velocity along spatial and temporal domain.
Slope of white lines corresponds to bubble velocity.

Based on the two groups of bubble data selected in Figure 3.3 indicated by white lines, the two calculated group velocities are – 62.9 mm/s and – 72.0 mm/s. The Doppler measured velocities for bubbles in the groups range from – 90 ~ – 100 mm/s. The difference between the local group velocities and the individual velocity is approximately – 20 ~ – 30 mm/s. The associated bubble diameter based on Stokes rise velocity models are 0.12 mm based on slope in Figure 3.3 and 0.14 mm based on velocities from the Doppler measurement.

Group velocity and individual bubble rise velocity can be described by the void wave model for bubbly flow as [28]:

$$a_+ = (1 - n\alpha_0)u_r + u_l \tag{4}$$

where α is the void fraction, u_r is the relative velocity, u_l is the velocity of the liquid and n is a theoretical non-dimensional number [29]. Based on the momentum equation the relative velocity is given by:

$$u_r = \left(\frac{4g(1-\rho_g^*)(1-\alpha)\overline{D}}{3C_D} \right)^{1/2} \tag{5}$$

where $\overline{D}$is the mean diameter and ρ_g^* is defined as $\frac{\rho_g}{\rho_l}$. The coefficient of drag can be modeled as [30]:

$$C_D = 24\frac{1+0.1\mathrm{Re}_b^{3/4}}{\mathrm{Re}_b} \tag{6}$$

Combining the equations above, the relative velocity becomes [31]:

$$u_r = \left(\frac{g\left(1-\rho_g^*\right)(1-\alpha)\overline{D}}{18} \frac{\mathrm{Re}_b}{1+0.1\mathrm{Re}_b^{3/4}} \right)^{1/2} \tag{7}$$

where,

$$\mathrm{Re}_b = \frac{2\rho|u_r|\overline{R}_b}{\mu_l}\alpha_l^{2.5\mu^*} \tag{8a}$$

$$\mu^* = \frac{\mu_g + 0.4\mu_l}{\mu_g + \mu_l} \tag{8b}$$

such that μ is the viscosity and $\overline{\mathrm{R}}_\mathrm{b}$ is the mean radius of the bubbles.

The equations (7, 8) require a numerical method for solutions since the Reynolds Number Re_b is dependent on u_r, the relative velocity. Bases on values of void fraction α ranging from 0.01 to 0.1 and bubble diameters of 0.01 to 1 mm, the relative velocity is shown in Figure 3.4. Base on the figure below, the expected difference in velocity for a void fraction of 1% and observed rise velocity difference of 20 mm/s suggest a bubble diameter in excess of 1 mm, in contrast to the diameter calculated from Stokes rise velocity. The void wave velocity a_+ for a void fraction of 1% and bubble diameter of 1 mm where in equation (4) n = 1.95 based on calculation with $u_l \approx 0$ is then a_+ = 14.7 mm/s. It is suggested that for typical bubbly flow with interfacial drag, n = 1.75 [29]. This may be due to the fact that bubbles are active reflectors and possibly distorting the Doppler frequency at the interface.

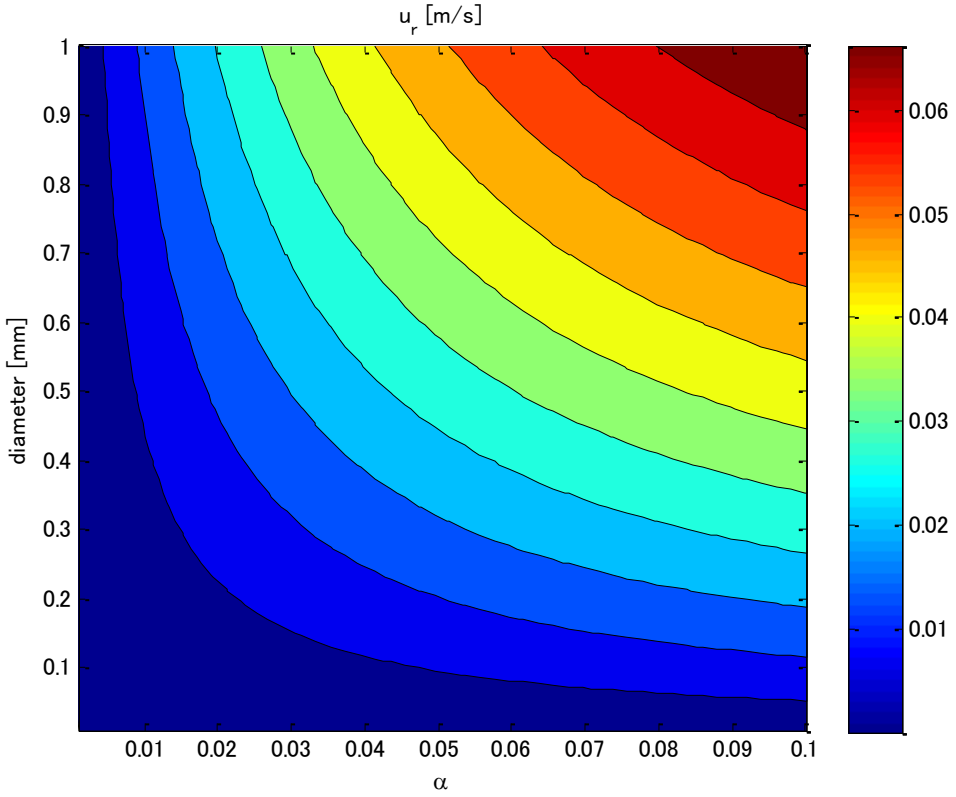

Figure 3.4: Contour of relative velocities

The void fraction can be calculated by solving for void fraction α in equation 4, in conjunction with parameters defined in equation 5 through equation 8. Employing an iterative numerical method where the bubble diameter is 0.4 mm and using the measured Doppler velocities, the void fraction α = – 0.146 is obtained. This is physically contradictory, however if u_l is taken into account a solution can be found when $u_l \geq 0.05$ (5 cm/s) with α = 0.153. Since mercury flow inside the stainless steel cylindrical tank is being circulated by the pump some liquid velocity, u_l ,is expected, but no independent measurement of liquid velocity is made in the measurement volume for these experiments. However, accurate void fraction measurements may be possible by refining this comparison of the individual bubble rise velocity to the group velocity.

3.2 Ultrasound

3.2.1 Microbubbles in Water

The stainless steel microbubbler described in Figure 2.16 was tested in water. The microbubbler was placed in an aquarium for testing as shown in Figure 3.5, below. The objective of the test was to optically measure the performance of the bubbler before testing in mercury.

Figure 3.6 below is a close up image of the microbubbler head generating bubbles. The majority of the bubbles are of order 100 µm in diameter. In addition to confirming the working condition of the device, this examination also shows the invariance of the elongation of the bubbler body design on the microbubble production.

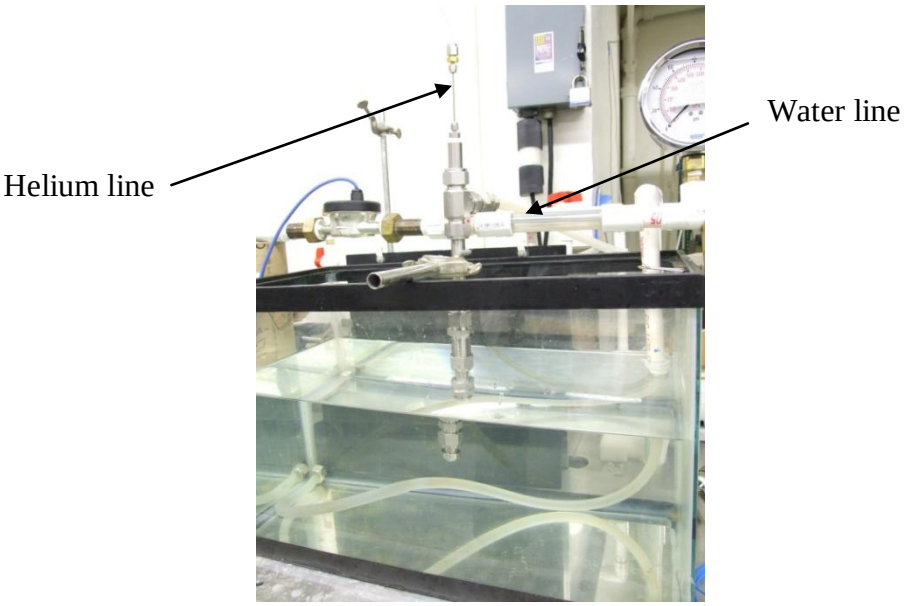

Figure 3.5: Microbubbler testing inside water loop.

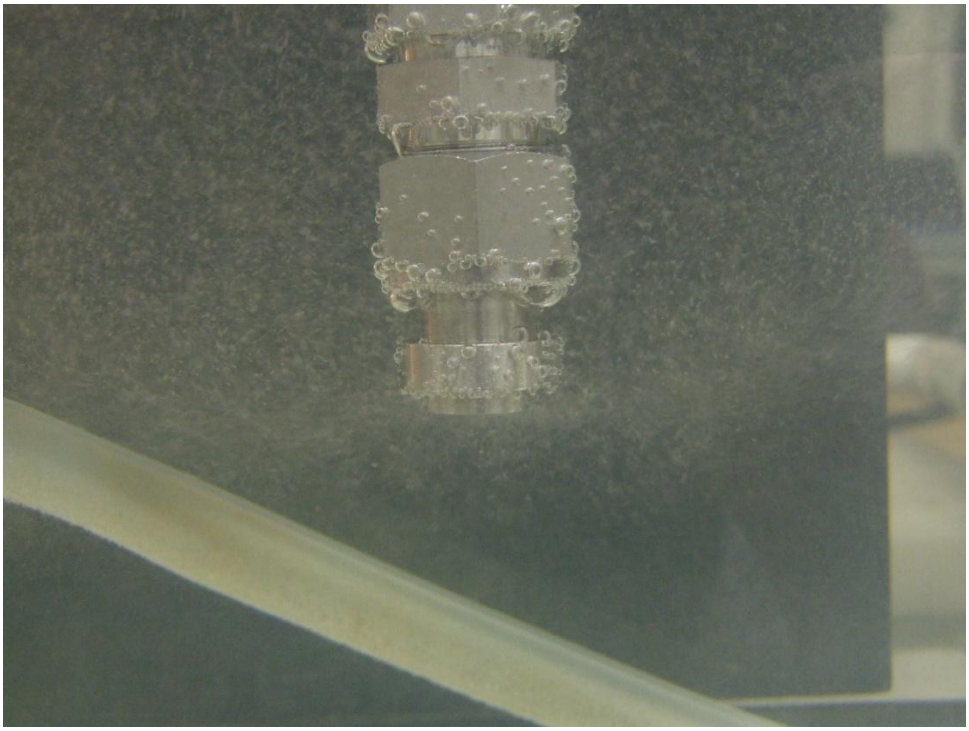

Figure 3.6: Microbubbler tip under operation.

The bubbles in the US Figure 3.7 appear larger, but are microbubbles nearly identical to those in Figure 3.6, with diameter near 100 μm. The image of bubbles in Figure 3.7 is clearest between 2.0 to 3.5 cm where the focus, marked in magenta, is set. The Image beyond the focused region degrades rapidly, becoming almost a smear at maximum range of 7 cm.

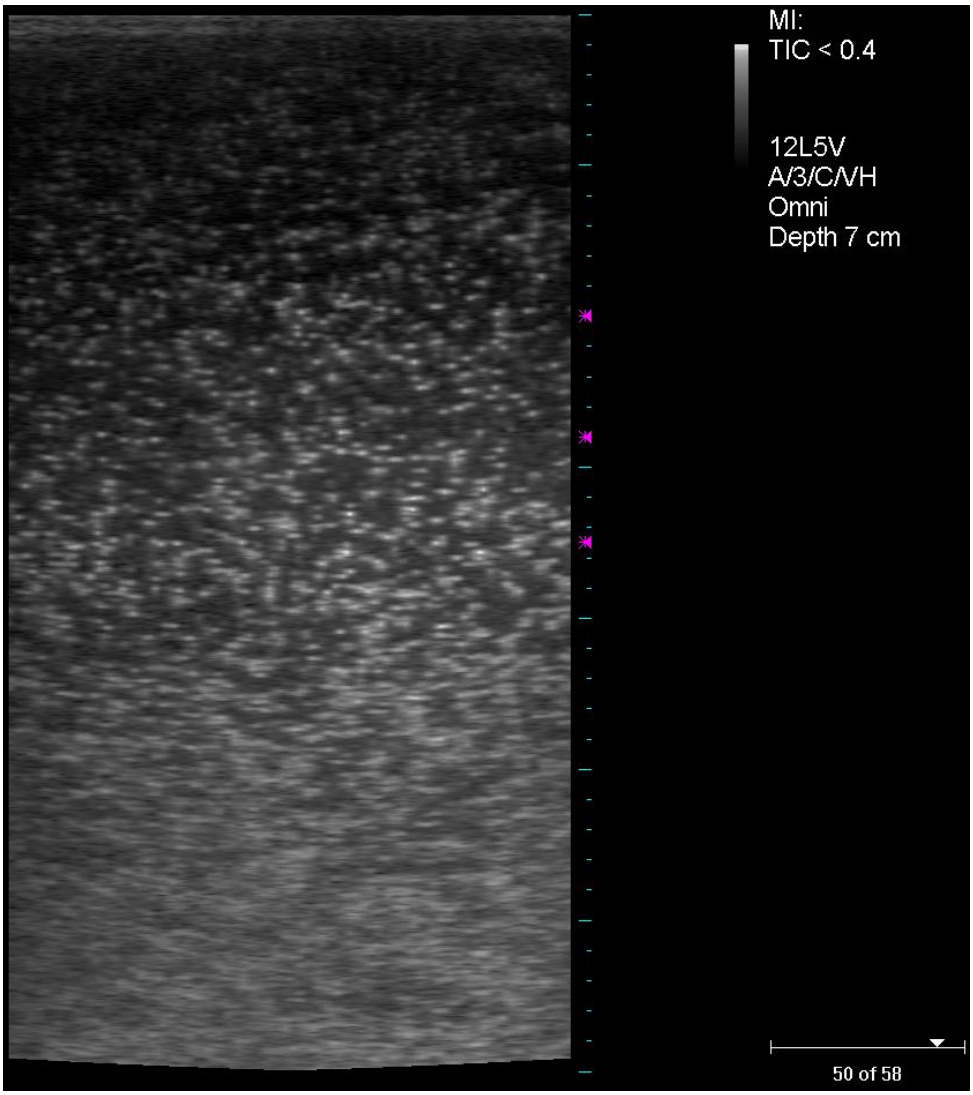

Figure 3.7: Microbubbles in water.

Under the same conditions as for Figure 3.7, M-mode was used to observe rising bubbles in Figure 3.8. The two images are B-mode on the top and the M-mode on the bottom. The y-axis represents the depth and x-axis is time. Thus, this bottom figure describes the rise velocity of microbubbles in water. The bubbles are almost identical in diameter as seen in the actual image of Figure 3.6. The rise velocity of the bubbles based on the slope is approximately 0.67 cm/s. Based on this rise velocity the bubble diameter is calculated to be 100 μm using Stokes solution which is consistent with visual observation.

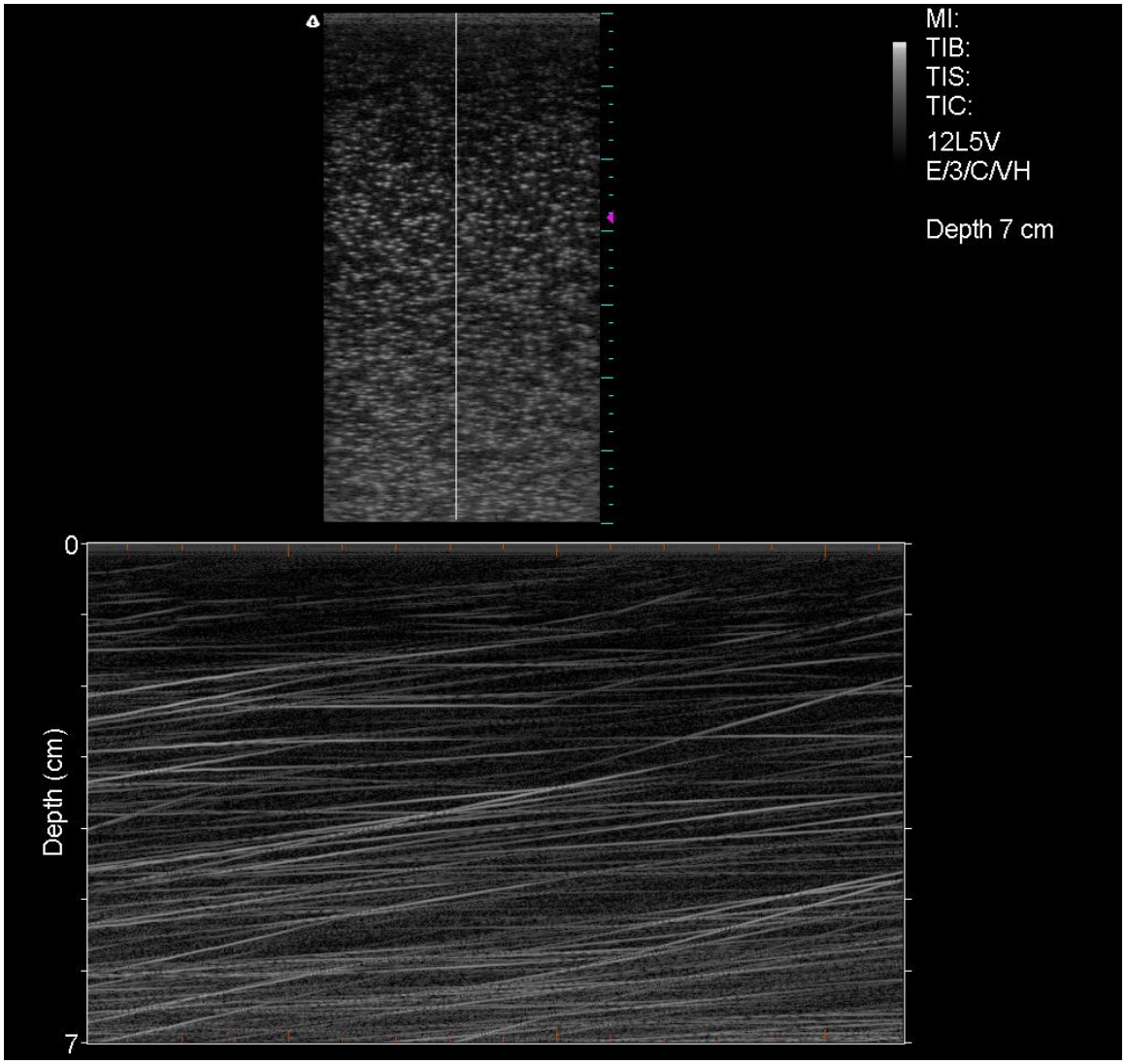

Figure 3.8 Use of M-mode on rising bubbles with time span of 3 sec.

US experiences image quality loss due to attenuation of signal when bubbles collect on the transducer head. The accumulation of bubbles creates a layer of air between the US surface and water, attenuating the signal into air (0.1% of the acoustic energy is transmitted based on the transmission coefficient). Figure 3.9 data show influence of bubbles partially covering the US probe surface. This figure will otherwise be similar to Figure 3.8 if bubbles were not present on the surface.

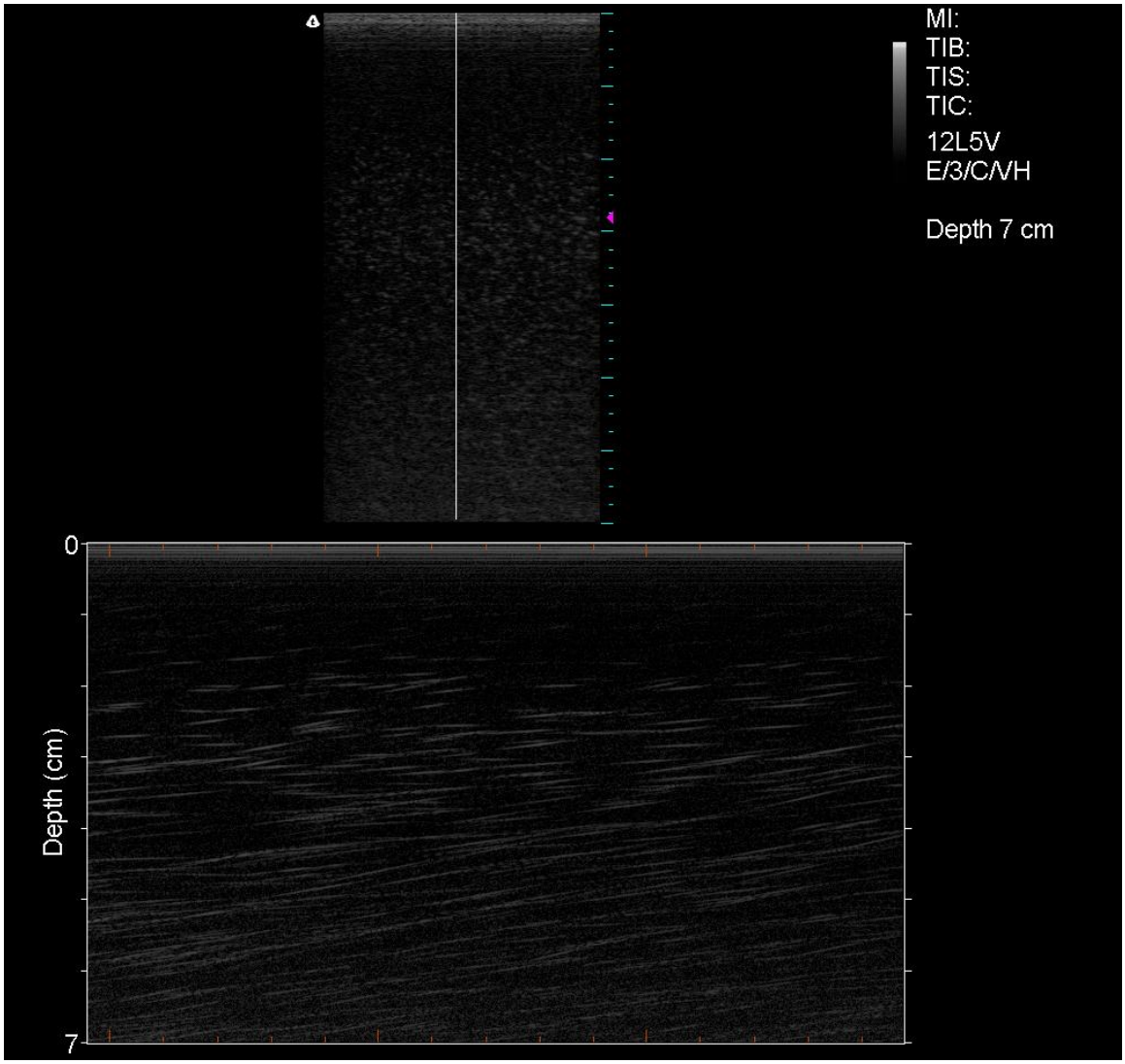

Figure 3.9: Scan result as bubbles accumulate on the transducer surface of the ultrasound probe.

3.2.2 Bubbles in Mercury

Mercury sealed inside a stainless-steel tank was injected with helium bubbles, similar to the UVP bubble generation except without homogenization. The US probe was oriented in a manner shown in Figure 3.10. Figure 3.11 shows the bubbles rising across the US field. Due to the cylindrical shape of the tank, US conforming gel was used between the US probe and stainless-steel tank. The gel and stainless-steel tank surface is present as two streaks seen on the left side of Figure 3.11. The bubbles produced in this

manner were several mm in diameter, as determined using passive acoustic techniques and mass flow measurement [32].

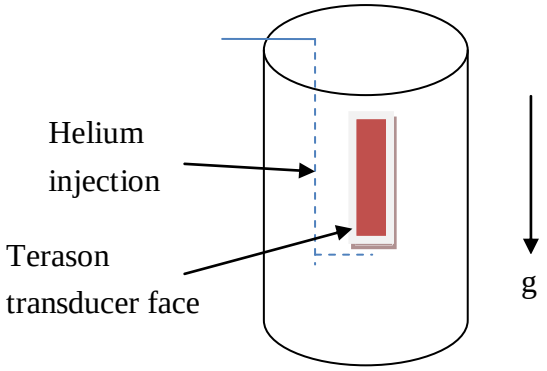

Figure 3.10: Schematics of cylindrical tank with gas injection tube (blue line).

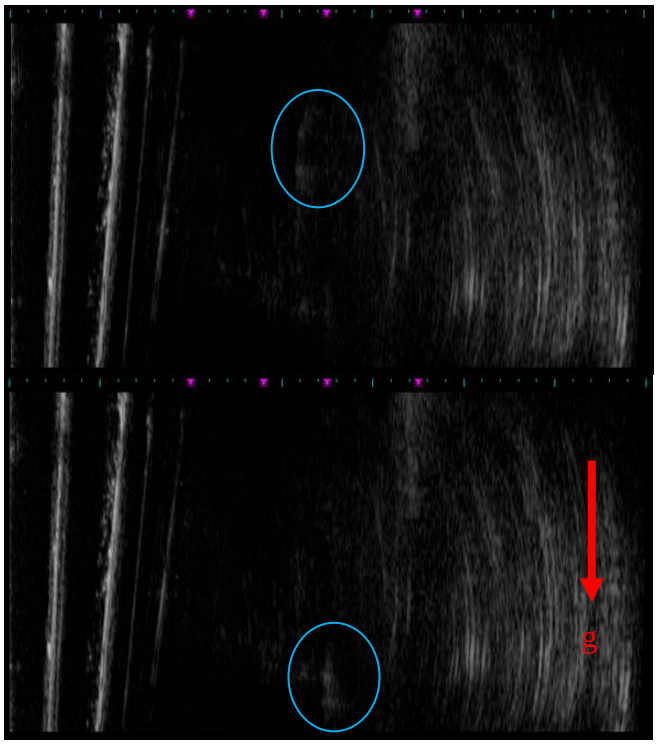

Figure 3.11: The bottom frame with bubble(s) encircled in blue.
The top frame is the next frame following the same bubble(s).

3.2.3 Microbubbles in Mercury

Figure 3.12 through Figure 3.16 are consecutive frames of microbubbles in mercury. US is able to detect bubbles in mercury for certain bubble diameters. Bubbles are visible in a region spanning 3 ~ 4 cm. Unlike microbubble images in water, the image quality in mercury is typical of the images in Figure 3.12 through Figure 3.16. The transducer is optimized for tissue, with acoustic properties similar to water, with acoustic impedance, density times sound speed, equal to 1.4 x 10^6 Kg/s-m^2. Mercury sound speed is similar to that in water, but the density is 13.5 times greater, resulting in impedance equal to 18.9 x 10^6 kg/s-m^2. The acoustic energy transmitted into the mercury is determined by the transmission coefficient, given by:

$$T_{coef} = 1 - \left(\frac{Z_2 - Z_1}{Z_1 + Z_2} \right)^2 \tag{9}$$

where Z is the impedance of the material. For the bubble images below where a layer of gel is present the transmission coefficient is 0.26. In the case where a layer of gel and stainless steel are present, the transmission coefficient into mercury is 0.10. Therefore, the ability to detect the echo is greatly reduced in mercury.

The acoustic intensity is proportional to the square of the pressure amplitude, with instantaneous intensity given by:

$$i = \frac{p_i^2}{\rho c} \tag{10}$$

where p_i is the instantaneous acoustic pressure, c the velocity of sound and ρ the density. Oscillations in pressure often make time-averaged intensity more of an interest than instantaneous intensity. Time-averaged intensity over one cycle is given by:

$$I = \frac{p_0^2}{2\rho c} \tag{11}$$

where p_0 is the peak pressure amplitude.

Intensity of ultrasonic beam is rarely measured in absolute terms. The reduction in intensity is described as a relative measurement expressed in decibels (dB) as:

$$Level = 10\log_{10}\left(\frac{I}{I_0}\right) \tag{12}$$

The reference intensity I_0 is often the intensity of the transmitted ultrasound.

Figure 3.12: Microbubbles in Mercury frame 2.

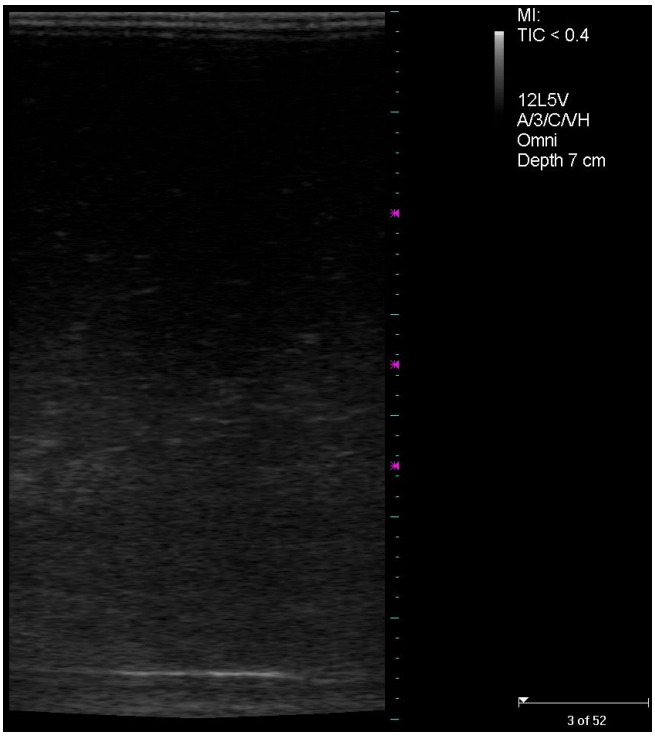

Figure 3.13: Frame 3.

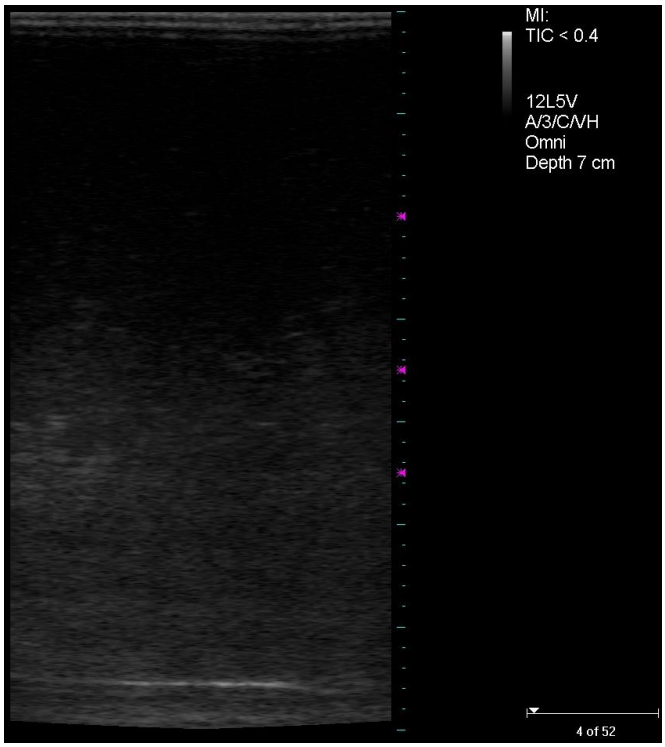

Figure 3.14: Frame 4.

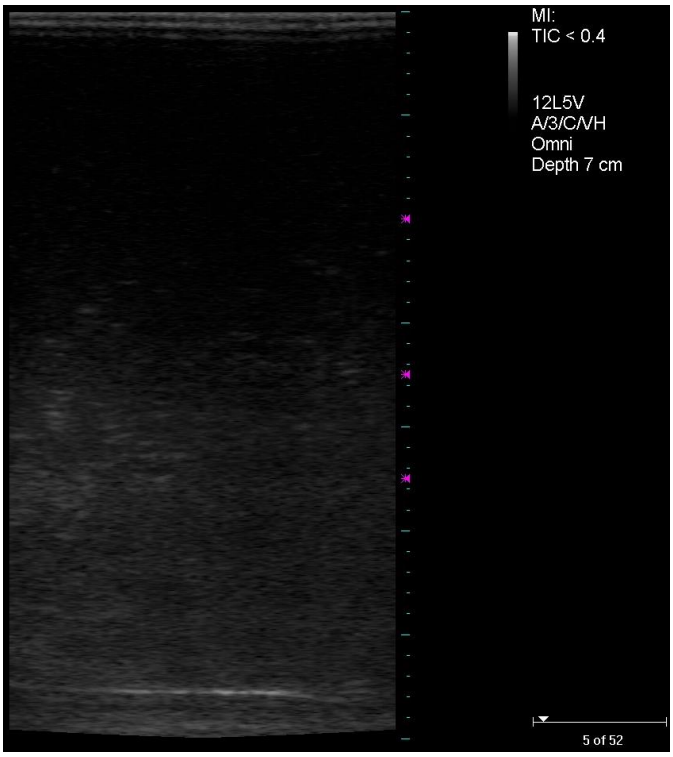

Figure 3.15: Frame 5.

Figure 3.16: Frame 6.

In a separate experiment with the same setup, microbubbles in mercury were imaged once more. Figure 3.17 and Figure 3.18 are successive frames with bubbles encircled in blue in some of the frames. Image quality is relatively poor compared to the study described in Figure 3.12 through Figure 3.16. This is mainly due to the poor acoustic energy transmission between the US head and mercury as the echoes across the top in Figure 3.17 and Figure 3.18 show. These echoes are likely due to the presence of small bubbles inside the layer of acoustic gel used to couple the transducer to the mercury.

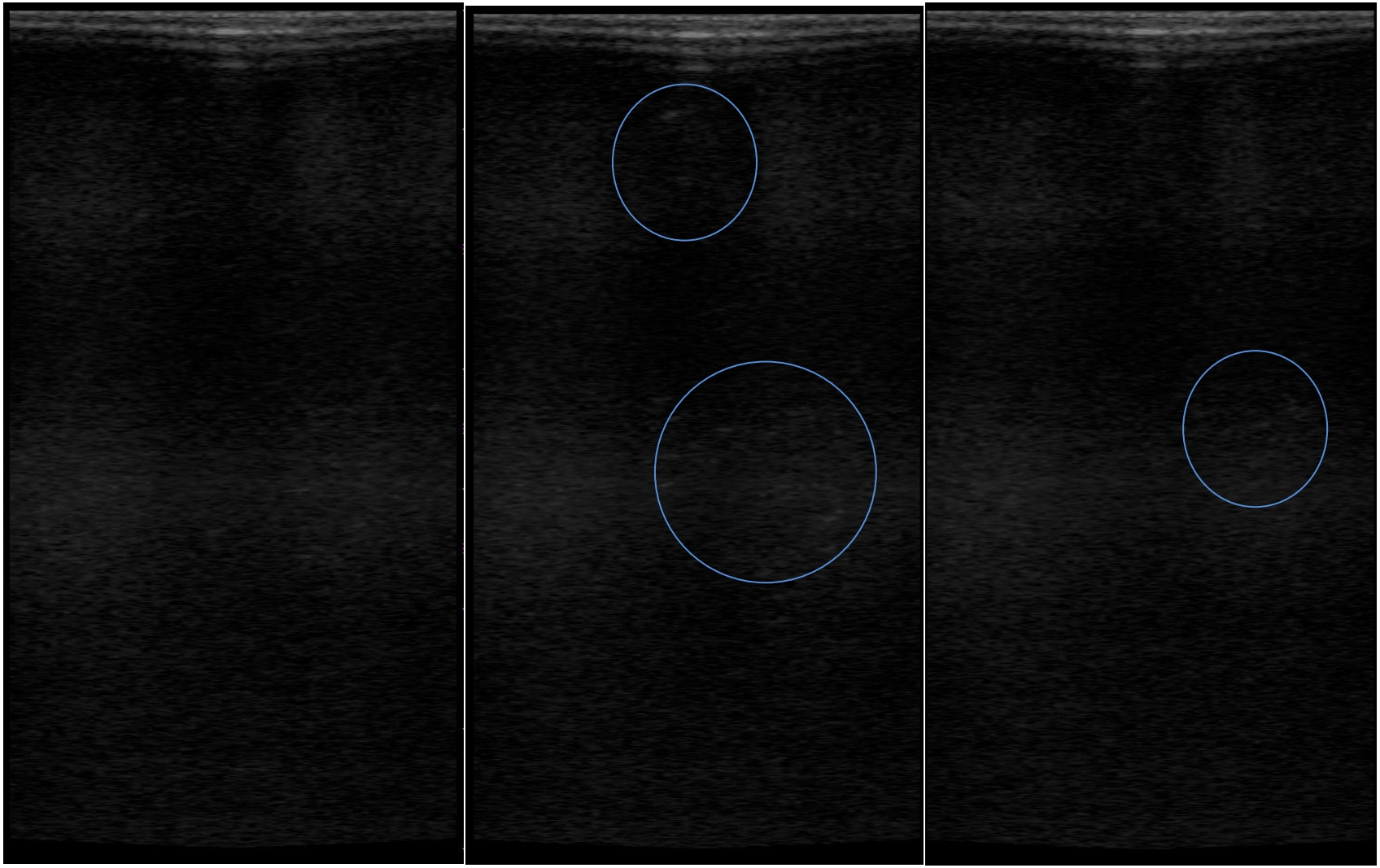

Figure 3.17: Consecutive images of bubbles in mercury starting on the left.

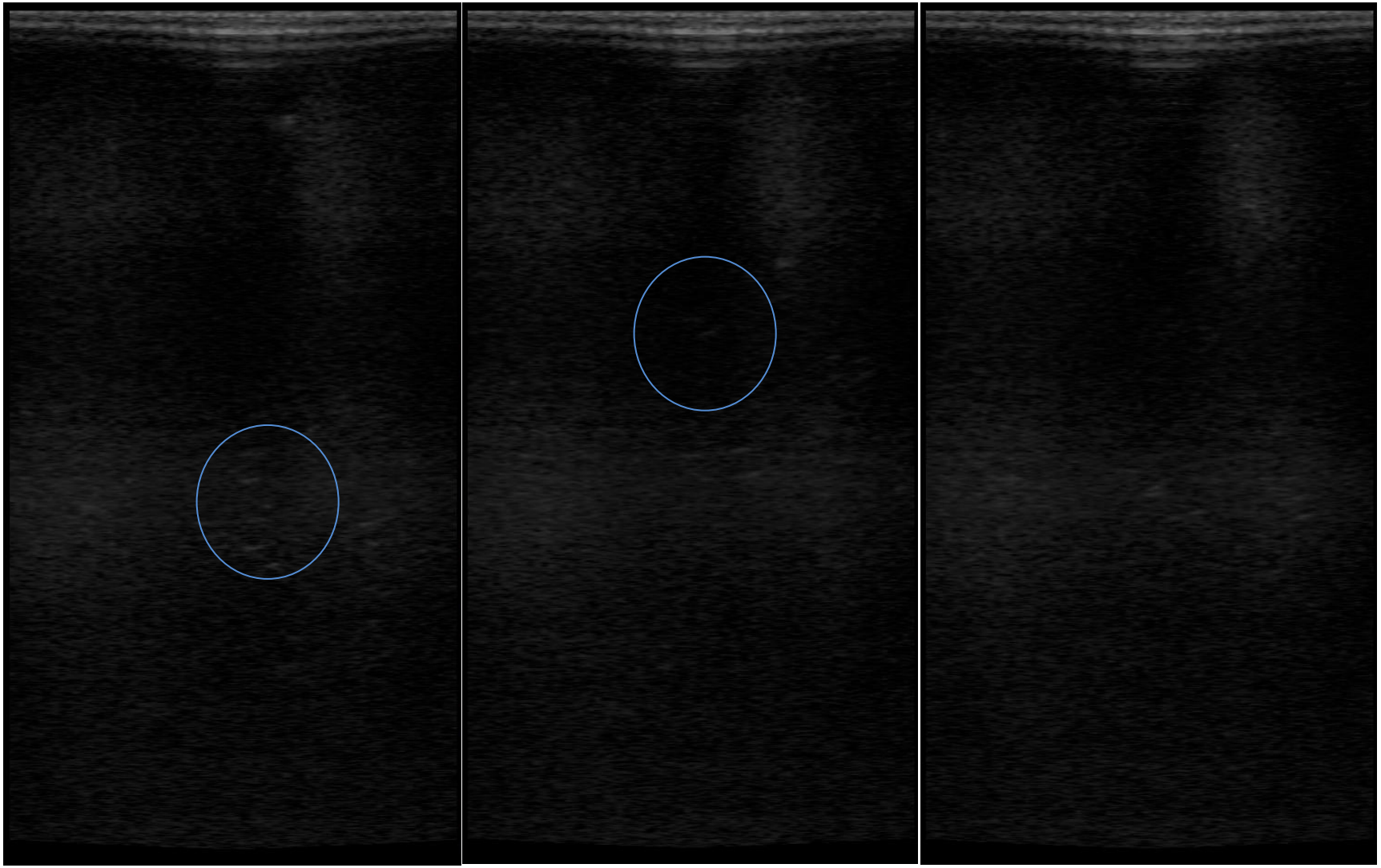

Figure 3.18: Consecutive images of bubbles in mercury starting on the left.

Based on two frames of Figure 3.17 (center and right), a PIV was performed. The contrasts of frames were enhanced to improve the distinction of bubbles from background. Figure 3.19, below shows the calculated velocity field. PIV was not possible for the other frames due to poor image.

Figure 3.17 and Figure 3.18 contain frames with dark shadows, similar to those highlighted (in blue) in Figure 3.20. Bubble(s) adhering to surface absorb the transmitted signal creating an appearance of void. The strong signal along the left side of the image in Figure 3.20 is the microbubbler head.

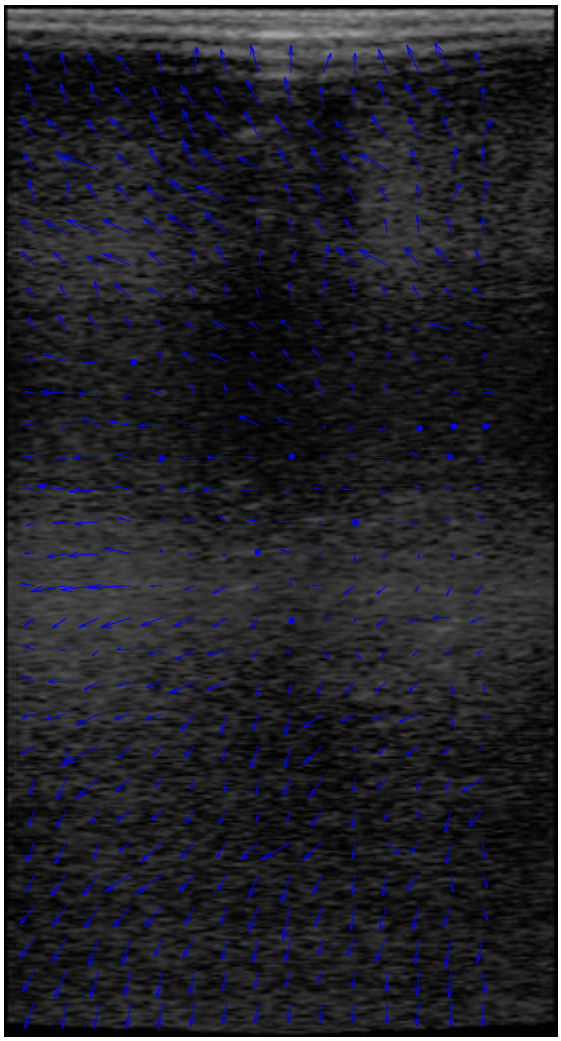

Figure 3.19: PIV based on the center and right frames of Figure 3.17.

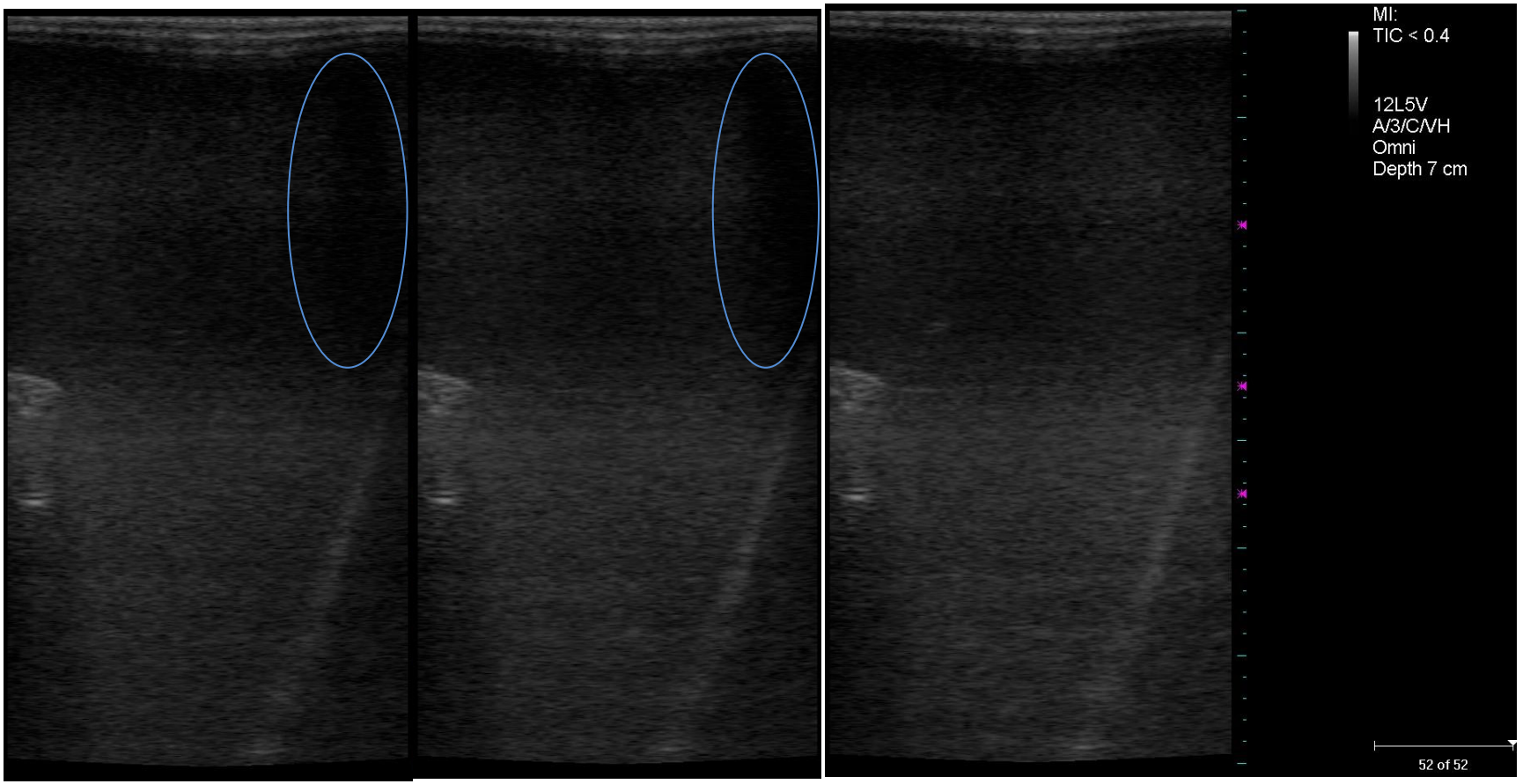

Figure 3.20: Three consecutive frames (left to right) of bubble casting shadow.

Chapter 4 : CONCLUSION

4.1 Overview

Cavitation damage inside the mercury target vessel diminishes the service life. Damage rate is reduced by providing compressibility to the mercury target material through the addition of small gas bubbles. This research examines the application of ultrasound techniques for bubble characterization in water and mercury. An Ultrasound velocity profiler (Met-Flow UVP) was used in static liquid to measure rise velocities for helium bubbles in mercury and microbubbles in water. Direct measurement of bubble velocity using the UVP enables the characterization of bubble diameter through the use of bubble rise velocity models.

Medical Ultrasound can also provide useful data as it provides 2-D images of bubbles in a 30 frame per second video stream. The medical ultrasound images are somewhat distorted, but velocity measurements are possible from the images when corrections are applied. The US imaging system also operates in a Doppler mode, allowing direct measurement of rise velocity when the transducer is positioned looking downward.

Ultrasonic imaging methods return echoes when solid targets are of diameter greater than ¼ wavelength. Since our maximum drive frequency was near 12 MHz, the minimum detectable diameter was near 100 μm. Rise velocity data and optical data indicate that in the case of bubbles, echoes are detected even when the bubble diameter is well less than ¼ wavelength. This is likely due to the compliant and reactive nature of the bubble, which has a resonant frequency defined as [33]:

$$\varpi^2 = \frac{3\gamma P}{d^2 \rho} \tag{13}$$

where $\omega = 2\pi f$, with frequency f , diameter d, density of the medium ρ, ratio of specific heats γ and static pressure P.

The compliant surface of the bubble may also distort the Doppler response, and bias the rise velocity values measured using the Doppler frequency shift. However, velocities determined from time of flight, and the Doppler derived velocities were consistent within 15% for the cases examined here.

This study presented the rise velocity measurements for bubbles in water and mercury. Bubbles of 100 μm diameter were found from rise velocities of 25 mm/s for microbubbles in water. Mercury bubbles of 100 μm diameter were measured with rise velocity of 65 mm/s. The velocity for bubble groups follows void wave theory, and a method for group velocity measurement in bubbly flow using ultrasound is developed. The void wave model with measured bubbled diameter and measured group velocity may allow for the characterization of void fraction with improved resolution of liquid velocity parameters.

4.2 Future work

Medical ultrasound images are distorted and require correlation of their image field to optical observation to facilitate engineering flow measurement. Maximum frame rate in current US imaging systems extends to 200 frames per second. Improvements in transducer design and image handling can make 2-D US imaging systems an engineering tool for flow measurement. Special US imaging transducer heads suited to high temperature and dense fluids could be useful to liquid metal reactor refueling operations and fabrication of opaque materials such as metals and plastics for injection molding, and processing of metal foams.

LIST OF REFERENCES

[1] UT-Battelle. ORNL Neutron Sciences. [Online]. http://neutrons.ornl.gov/facilities/SNS/proposed-upgrades.shtml

[2] UT-Battelle. ORNL Neutron Sciences. [Online]. http://neutrons.ornl.gov/images/sns_target_2005.jpg

[3] G.S. Bauer et al. (Eds.), "The ESS Technical Study, The European Spallation Source Study," 090 237 659, 1996.

[4] H. Lengeler, "The European Spallation Source study (ESS)," in *Proceedings of the ICANS-XIII Conference*, 1995, p. 819.

[5] L. K. Mansur, T. A. Gabriel, J. R. Haines, and D. C. Lousteau, "R&D for the Spallation Neutron Source mercury target," *Journal of Nuclear Materials*, vol. 296, no. 1-3, pp. 1-16, 2001.

[6] J.R. Haines et al., "Summary of cavitation erosion investigations for the SNS mercury target," *Journal of Nuclear Materials*, vol. 343, no. 1-3, pp. 58-69, August 2005.

[7] B.W. Riemer, "Mitigation of Cavitation Damage in Liquid," 2009.

[8] M. F. Francis and A. E. Ruggles, "Helium Bubble Injection Solution to the Caviation Damage," in *CAARI*, 2008.

[9] Sang-Joon Lee and Guk-Bae Kim, "X-ray particle image velocimetry for measuring quantitative flow information inside opaque objects," *Journal of Applied Physics*, vol. 94, pp. 3620-3623, 2003.

[10] J. N. Koster, T. Seidel, and R. Derebail, "A radioscopic technique to study convective fluid dynamics in opaque liquid metals," *Journal of Fluid Mechanics*, vol. 343, pp. 29-41, 1997.

[11] T. Hibiki et al., "Visualization of fluid phenomena using a high frame-rate neutron radiography with a steady thermal neutron beam," *Nuclear Instruments and Methods in Physics Research A*, vol. 351, no. 2-3, pp. 423-436, December 1994.

[12] B. W. Riemer, P. R. Bingham, F. G. Mariam, and F. E. Merrill, "Measurement of Gas Bubbles in Mercury Using Proton Radiography," in *AccApp'07*, Pocatello, 2007, pp. 531-537.

[13] M. Berke. (2000, September) Nondestructive Testing. [Online]. http://www.ndt.net/search/link.php?id=540&file=article/v05n09/berke/berke.pdf

[14] T. Aastroem, "From Fifteen to Two Hundred NDT-methods in Fifty Years," in *17th World Conference on Nondestructive Testing*, Shanghai, 2008.

[15] Met-Flow SA, *UVP Monitor User guide*. Lausanne, Switzerland, 2000.

[16] Y. Takeda, "Development of an ultrasound velocity profile monitor," *Nuclear Engineering and Design*, pp. 227-284, 1991.

[17] G. Watts, "John Wild," *BMJ*, vol. 339, no. b4428, Oct 2009.

[18] I. Donald, J. Macvicar, and T. G. Brown, "Investigation of abdominal masses by pulsed ultrasound," *Lancet*, vol. 1, no. 7032, pp. 1188-1195, Jun 1958.

[19] J. Woo. (2002) ob-ultrasound.net. [Online]. http://www.ob-ultrasound.net/history1.html

[20] J. R. Lindner, "Microbubbles in medical imaging: current applications and future directions," *Nature Reviews Drug Discovery*, vol. 3, no. 6, pp. 527-32, June 2004.

[21] J. R. Lindner, J. Song, A. R. Jayaweera, J. Sklenar, and S. Kaul, "Microvascular rheology of Definity microbubbles following intra-arterial and intravenous administration," *J Am Soc Echocardiogr*, vol. 15, no. 5, pp. 396-403, May 2002.

[22] Wei K et al., "Quantification of myocardial blood flow with ultrasound-induced destruction of microbubbles administered as a constant venous infusion," *Circulation*, vol. 97, no. 5, pp. 473-483, Feb 1998.

[23] R. Bekeredjian, P. A. Grayburn, and R. V. Shohet, "Use of ultrasound contrast agents for gene or drug delivery in cardiovascular medicine," *Journal of the American College of Cardiology*, vol. 45, no. 3, pp. 329-335, Febuary 2005.

[24] F. C. Laing and A. B. Kurtz, "The Importance of Ultrasonic Side-Lobe Artifacts," *Radiology*, pp. 763-768, 1982.

[25] W. R. Hedrick, D. L. Hykes, and D. E. Starchman, *Ultrasound Physics and Instrumentation*. St. Louis: Elsevier Mosby, 2005.

[26] Teratech Corp., Terason Ultrasound System User Guide, 2008.

[27] S. Walker and A. E. Ruggles, "Mercury Scaling of a Swirling Jet Micro-Bubble Generator," in *ASME Fluids Engineering Division Summer Meeting*, Montréal, Canada, 2010, pp. ICNMM2010-30534.

[28] J-W. Park, D.A. Drew, R.T. Lahey Jr., and A. Clausse, "VOID WAVE DISPERSION IN BUBBLY FLOWS," *Nuclear Engineering and Design*, vol. 121, no. 1, pp. 1-10, July 1990.

[29] R.T. Lahey Jr., J-W. Park, and D.A. Drew, "The analysis of void waves in two-phase flow," *Nuclear Engineering and Design*, vol. 141, no. 1-2, pp. 203-224, June 1993.

[30] M. Ishii and N. Zuber, "Relative motion and interracial drag coefficient in dispersed two-phase flow of bubbles, drops and particles," in *Proc. AIChE 71st Annual Meeting*, Miami, FL, 1979.

[31] J.-W. Park, D.A. Drew, and R.T. Lahey Jr., "The measurement of void waves in bubbly two-phase flows," *Nuclear Engineering and Design*, vol. 149, no. 1-3, pp. 37-52, September 1994.

[32] Stuart A. Walker. (2010, May) An Investigation of Gas Bubble Generation and Measurement in Water and Mercury. [Online]. http://trace.tennessee.edu/utk_gradthes/668

[33] A.S. Dukhin and P.J. Goetz, *Ultrasound for Characterizing Colloids*. Amsterdam, Netherlands: Elsevier Science B.V., 2002.

APPENDIX

Appendix A: LabVIEW VI for Data Acquisition

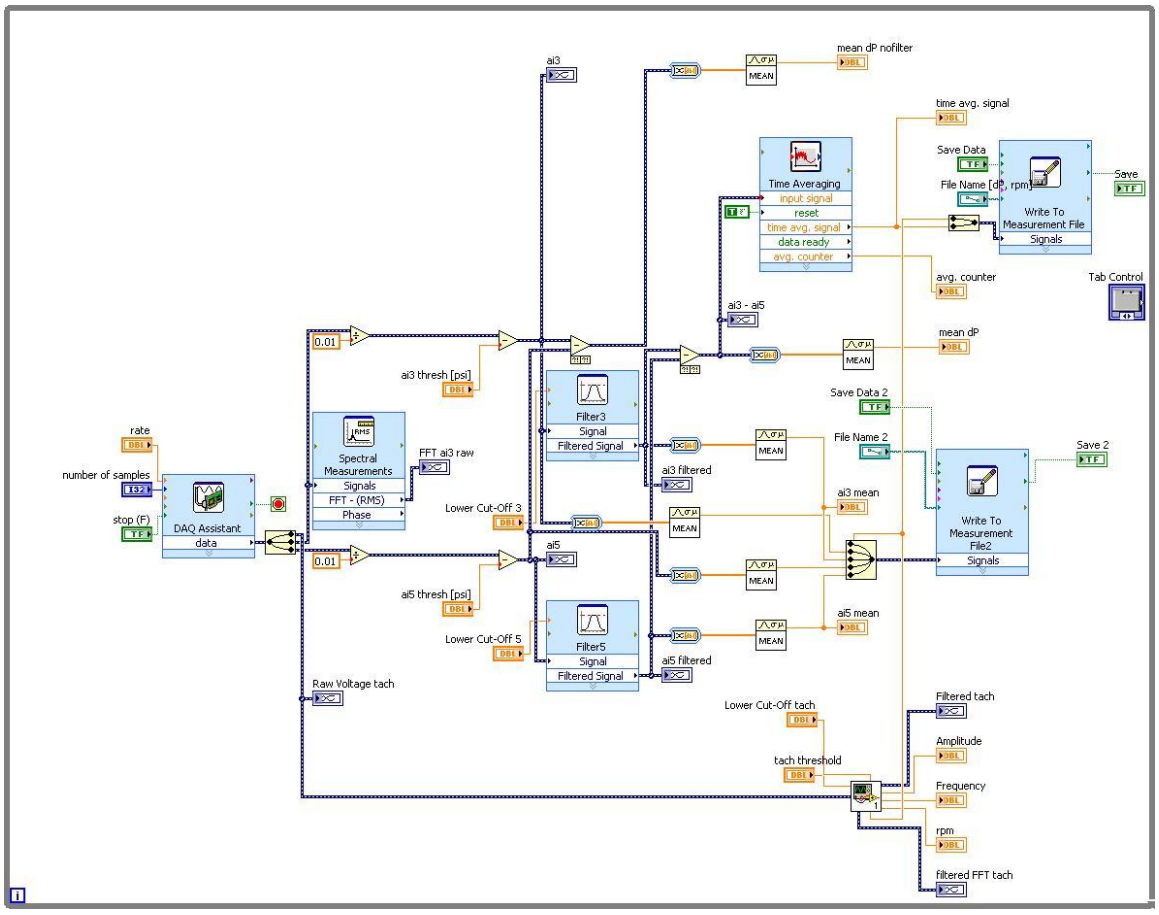

Figure A.1: LabVIEW block diagram for data acquisition on the mercury loop.

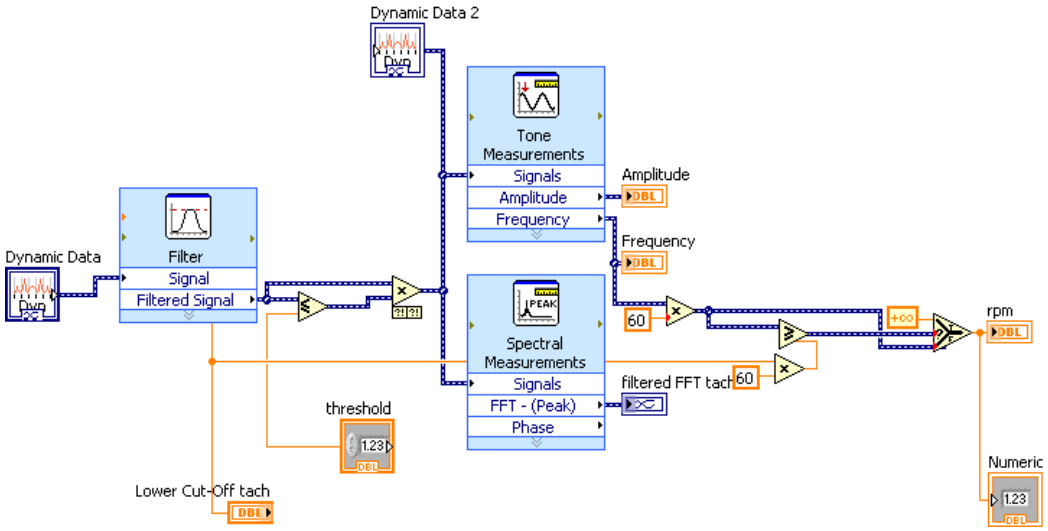

Figure A.2: LabVIEW block diagram for tachometer.

Appendix B: Experimental Procedure

Table B- 1: List of stainless steel fitting.

Part #	Quantity	Description
SS-1010-6-8	1	5/8 to 1/2 reducer
SS-1010-61	1	5/8 bulkhead
SS-1010-6	1	5/8 union
SS-1013-1	5	5/8 front ferrule
SS-1014-1	5	5/8 back ferrule
SS-1012-1	3	5/8 nut
SS-T10-S-065-20	20ft	SS316 5/8 pipe

Experimental Procedure for Mercury –Microbubbler

Equipments

Safety
- ☐ Disposable bags (ziplock, large)
- ☐ Hazardous waste container
- ☐ Goggles/safety glasses
- ☐ Mercury vapor monitor
- ☐ Disposable gloves
- ☐ Mercury spill kit
- ☐ Lab coat
- ☐ tape

Testing
- ☐ microbubble test section
- ☐ lid
- ☐ Wrench
- ☐ cap

US
- ☐ Terason Unit
- ☐ Acoustic gel
- ☐ Laptop
- ☐ Disposable bag/plastic wrap

Procedure

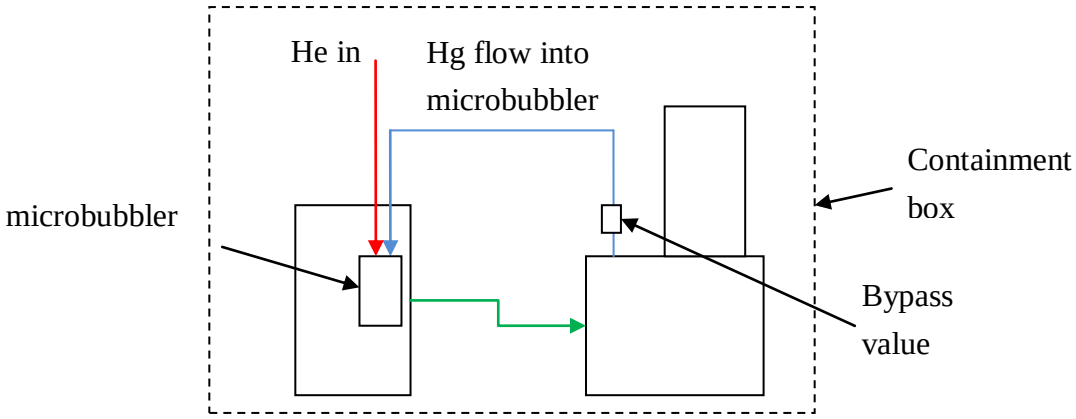

Safety

1. Put on lab coat, gloves and eye protection
2. Place mercury spill kit in readily accessible location
3. Start ventilation and vacuum pump to Hg loop box (remove potential vapor)
4. Remove tape and box cover (Hg loop containment)
5. Measure Hg vapor around loop. IF safe proceed, ELSE reseal box, close fume hood.

Check working system

1. Connect power cable to electrical outlet (240V)
2. Turn power down to 0%
3. Turn power on (Green indicator)
4. Open bypass valve, helium outlet valve
5. Slowly run up power to 100%, run for a few minutes. IF any leak is observed power down.
6. Close bypass value, repeat previous step
7. Visually check for Hg flow in test tank
8. Turn off power, open bypass value

Swap

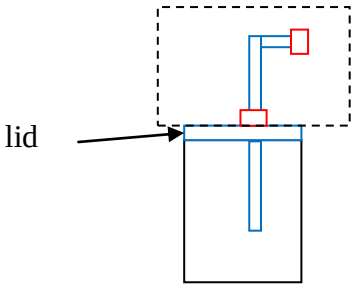

1. Remove Helium vent and inlet lines on lid
2. Remove lid clamp
3. Get plastic bag (large)
4. Remove top portion of pipe (dashed box, two bolts in red), use plastic bag to catch possible mercury leak while loosening bolts
5. Put removed pipe in the plastic bag
6. Lift and remove the lid, place it into the plastic bag
   * microbubble test section are in two part, similar to the figure above
7. Place new lid into the tank
8. Bolt top section of pipe (similar to the removal of the old pipe)

US benchmark measurement

* no Hg flow

1. Turn Terason unit on
2. Open access to Hg on lid
3. Cover US probe with plastic wrap (acoustic gel maybe necessary, check image quality)
4. Place US probe into Hg.
5. Set Terason for optimal setting
6. Remove treason, place it temporary in plastic bag
7. Close access to Hg

Flow test – Test microbubbler

1. Close bypass value
2. Turn on power to motor.

3. Slowly run up power to 100%, Open Helium line. Run for a few minutes. IF any leak is observed power down.
4. Visually observe for rising bubble
5. Power down and turn off motor.

US with flow with bubbles

1. Open access to Hg on lid
2. Place US probe into Hg
3. Turn on power to motor
4. Slowly run up power to 100%, Open Helium line. IF any leak is observed power down.
5. Check Hg vapor level.
6. Acquire US image as necessary.

Clean Up

1. Turn off power and unplug power cable
2. Open bypass value
3. Remove Terason
4. Repeat Swap step above to restore original setup
5. Check and Clean any mercury spills
6. Check for mercury vapor
7. Seal containment box using tape
8. Close fume hood and turn off ventilation.

Appendix C: DICOM file conversion by MATLAB

Matlab script for converting DICOM files (*.dcm) to still images or AVI files.

dicom2media.m

```
% Hiraku Nakamura
% 9 Nov 2009
% update: 20 Jan 2010
% DICOM import -> image | movie

clear;clc;
%cd 'C:\Programs\Teratech\Terason 3000\Image'
%cd 'J:\'
folder = '2010-02-02';
exten = '.dcm'; % file extention 4 char

l = ls(folder);
for i = length(l):-1:1
if (~strcmp(l(i,end-3:end), exten))
      l(i,:) = [];
end
end
for i = 1:length(l)
   fprintf(1,'\t %i %s\n',i,l(i,:))
end
i = input('import file #: ');
filename = l(i,:);    disp(['loading... ' filename])

info = dicominfo([folder '\' filename]);
[D4 map] = dicomread(info);
%% output
if isfield(info,'NumberOfFrames') == 0
   imshow(D4(53:end,:),map)
   imwrite(D4(53:end,:),map,[folder '\' filename(1:end-4) '.png'],'png')
else
for i = 1:info.NumberOfFrames
      imshow(D4(53:end,:,1,i));
      M(i) = getframe;
end
% create avi
%movie2avi(M,filename(1:end-4),'compression','None','quality',100)
   movie2avi(M,filename(1:end-4),'quality',100)
end

%% contour
for i = 1:info.NumberOfFrames
%     imshow(D4(62:749,125:403,1,i));
   imcontour(D4(62:749,125:404,1,i),20);
   title([num2str(i) '/' num2str(info.NumberOfFrames)]);
   M(i) = getframe;
end
movie2avi(M,filename(1:end-4),'quality',100)
```

```
%movie(M)
%title(['contour ' folder '\' filename])
```

VITA

Hiraku Nakamura was born in Okinawa, Japan on 26 August 1984. From August 2004 he attended Virginia Polytechnic Institute and State University (Virginia Tech) obtaining a Bachelor of Science in Aerospace Engineering in May 2008. From August 2008 he attended The University of Tennessee, Knoxville graduating with a Master of Science in Nuclear Engineering in December 2010.